

Microphysical time scales and local supersaturation balance at a warm Cloud Top Boundary

*Original*

Microphysical time scales and local supersaturation balance at a warm Cloud Top Boundary / Fossa', Ludovico; Abdunabiev, Shahbozbek; GOLSHAN KOVIJI, Mina; Tordella, Daniela. - In: PHYSICS OF FLUIDS. - ISSN 1070-6631. - ELETTRONICO. - 34:(2022). [10.1063/5.0090664]

*Availability:*

This version is available at: 11583/2964385 since: 2022-05-24T00:04:07Z

*Publisher:*

AIP

*Published*

DOI:10.1063/5.0090664

*Terms of use:*

This article is made available under terms and conditions as specified in the corresponding bibliographic description in the repository

*Publisher copyright*

(Article begins on next page)

# Microphysical timescales and local supersaturation balance at a warm cloud top boundary

Cite as: Phys. Fluids **34**, 067103 (2022); <https://doi.org/10.1063/5.0090664>

Submitted: 08 March 2022 • Accepted: 06 May 2022 • Accepted Manuscript Online: 10 May 2022 • Published Online: 02 June 2022

Ludovico Fossà,  Shahbozbek Abdunabiev,  Mina Golshan, et al.



View Online



Export Citation



CrossMark

## ARTICLES YOU MAY BE INTERESTED IN

### Coronavirus pleomorphism

Physics of Fluids **34**, 063101 (2022); <https://doi.org/10.1063/5.0094771>

### Assessing effectiveness and comfortability of a two-layer cloth mask with a high-efficiency particulate air (HEPA) insert to mitigate COVID-19 transmission

Physics of Fluids **34**, 061703 (2022); <https://doi.org/10.1063/5.0094116>

### Droplet formation simulation using mixed finite elements

Physics of Fluids **34**, 064105 (2022); <https://doi.org/10.1063/5.0089752>



APL Machine Learning

Open, quality research for the networking communities

MEET OUR NEW EDITOR-IN-CHIEF

LEARN MORE

# Microphysical timescales and local supersaturation balance at a warm cloud top boundary

Cite as: Phys. Fluids **34**, 067103 (2022); doi: [10.1063/5.0090664](https://doi.org/10.1063/5.0090664)

Submitted: 8 March 2022 · Accepted: 6 May 2022 ·

Published Online: 2 June 2022



View Online



Export Citation



CrossMark

Ludovico Fossà,<sup>a)</sup> Shahbozbek Abdunabiev,<sup>b)</sup> Mina Golshan,<sup>b)</sup> and Daniela Tordella<sup>b)</sup>

## AFFILIATIONS

Dipartimento di Scienza Applicata e Tecnologia, Politecnico di Torino, Corso Duca degli Abruzzi 24, 10129 Torino, Italy

<sup>a)</sup>Present address: Department of Mechanical Engineering, The University of Sheffield, S1 3JD Sheffield, United Kingdom.

<sup>b)</sup>Author to whom correspondence should be addressed: [daniela.tordella@polito.it](mailto:daniela.tordella@polito.it)

## ABSTRACT

Recent results have shown that there is an acceleration in the spread of the size distribution of droplet populations in the region bordering the cloud and undersaturated ambient. We have analyzed the supersaturation balance in this region, which is typically a highly intermittent shearless turbulent mixing layer, under a condition where there is no mean updraft. We have investigated the evolution of the cloud–clear air interface and of the droplets therein via direct numerical simulations. We have compared horizontal averages of the phase relaxation, evaporation, reaction, and condensation times within the cloud–clear air interface for the size distributions of the initial monodispersed and polydisperse droplets. For the monodisperse population, a clustering of the values of the reaction, phase, and evaporation times, that is around 20–30 s, is observed in the central area of the mixing layer, just before the location where the maximum value of the supersaturation turbulent flux occurs. This clustering of values is similar for the polydisperse population but also includes the condensation time. The mismatch between the time derivative of the supersaturation and the condensation term in the interfacial mixing layer is correlated with the planar covariance of the horizontal longitudinal velocity derivatives of the carrier air flow and the supersaturation field, thus suggesting that a quasi-linear relationship may exist between these quantities.

Published under an exclusive license by AIP Publishing. <https://doi.org/10.1063/5.0090664>

## I. INTRODUCTION

The large-scale dynamics of warm atmospheric clouds is closely coupled with small-scale phenomena. Lukewarm clouds are a stage of a complex interplay between competing turbulent and microphysical processes, which determine their evolution over time. However, many physical processes that are relevant for cloud dynamics have not yet been completely unraveled and still constitute a matter of debate in the cloud physics and turbulence communities. In recent years, a great deal of attention has been paid to the effect of turbulent mixing at cloud boundaries as well as its impact on droplet condensation (evaporation) and collision. The interfacial mixing of cloud and clear air has often been identified as the main cause of the observed broadening of droplet size distributions and the rapid onset of precipitation.

Warner<sup>1</sup> suggested the importance of mixing at a growing cloud top in unstable environments. Latham and Reed<sup>2</sup> and Baker *et al.*<sup>3</sup> were the first to recognize a difference between homogeneous and inhomogeneous mixing, where the microphysics timescale can be either longer or shorter than the timescale of the turbulent motions. The ratio between the turbulent timescale and the microphysical timescale is represented by the Damköhler number,  $Da$ . The same

turbulent flow encompasses a wide range of  $Da$  along the energy cascade.<sup>4</sup> Several timescales have been used to define the Damköhler number<sup>5</sup> and to parameterize the impact of the entrainment and mixing of clear air at cloud boundaries. These scales include evaporation, phase relaxation, and reaction timescales. The fundamental variable that drives the condensation (evaporation) of a droplet is supersaturation  $S = RH - 1$ , where  $RH$  is the relative humidity.<sup>6</sup>  $S$  varies over both time and space and is determined by the local, instantaneous concentration of water vapor  $\rho_v$  and temperature  $T$  through the Clausius–Clapeyron equation. However, supersaturation  $S$  has often been described as a somewhat global property of a cloud parcel,<sup>7</sup> and the local value of the vertical velocity and the microphysical properties are generally taken into account for its estimation. The supersaturation balance within a cloud is often described by means of a production–condensation model of the type proposed by Twomey,<sup>8</sup> where the mean updraft velocity  $w$  and the mean radius of the droplet population  $\bar{R}$  are the main contributors to the time derivative of  $S$

$$\frac{dS}{dt} \cong c_1 w - \frac{S}{\tau_{phase}}, \quad (1)$$

where  $\tau_{\text{phase}} = (c_2 n_d \bar{R})^{-1}$  is the phase relaxation timescale,<sup>9,10</sup>  $n_d$  is the droplet number density, and  $c_1$  and  $c_2$  are coefficients that depend, albeit only slightly, on the temperature,  $c_1$ , and temperature/pressure,  $c_2$ .<sup>11</sup> Cooper<sup>12</sup> described a theoretical framework in which the variability of  $S$ , and the subsequent broadening of the droplet size distribution is determined by the value of the integral radius as well as by the covariance of the integral radius and the vertical velocity fluctuation.

Sardina *et al.* generalized Twomey's model to a scalar transport equation that they used in their direct numerical simulation (DNS) study of cloud cores.<sup>13</sup> They showed that the contribution of the diffusive effect is negligible for large Reynolds numbers. Chandrakar *et al.*,<sup>14</sup> in a laboratory experiment, used the stochastic condensation model of Ref. 13 to investigate the effects of an aerosol concentration on the broadening of the droplet size distribution. They argued that supersaturation fluctuations determine diverse growth conditions inside cloud cores with low aerosol (and droplet) concentrations,<sup>15</sup> who studied the impact of turbulent temperature and water vapor density fluctuations on supersaturation by performing *in situ* measurements of shallow-cumulus clouds, suggested the same. Their data show a reduction in the standard deviation of supersaturation inside cloud cores compared to regions where few or no droplets are located. They used the phase relaxation time  $\tau_{\text{phase}}$  as the microphysical timescale in the Damköhler number. Prabhakaran *et al.*<sup>16</sup> used the stochastic condensation approach to study the activation of dry-sodium chloride aerosols as well as droplet nucleation and growth via laboratory experiments. They used a climate chamber where statistically steady-state Rayleigh–Bénard turbulence had been generated. They claimed that their results can be extended to a context in which the effects of entrainment and mixing are important, and that, in this case, droplet activation is governed by a fluctuation-dominated regime, even though such a region is subsaturated on the whole.

However, many DNS studies have focused on both statistically steady-state and transient shearless mixing layers located at a vertical droplet-laden, cloud–clear air interface.<sup>17,18</sup> Kumar *et al.*<sup>19</sup> investigated the effects of the range of the energy cascade on the relative dispersion of a droplet population, which was observed to increase for larger initial values of the domain size-based  $Da$ . Miller and Bellan<sup>20</sup> performed direct numerical simulations (DNS) of a droplet-laden shear layer that featured a two-way interphase coupling and a Lagrangian tracking system for the droplets. Onishi *et al.*<sup>21</sup> studied the influence of gravity on droplet collision and coalescence. Sidin *et al.*<sup>22</sup> used a synthetic turbulent field to investigate the impact of both large and small-scale turbulent eddies on droplet condensation and evaporation. Their DNS model did not take into account the effects of condensation and evaporation. Golshan *et al.*<sup>23</sup> have recently performed direct numerical simulations of a horizontal, droplet-laden, interfacial shearless mixing layer subject to unstable stratification. They observed a remarkable acceleration in the dynamics of the droplet population in the mixing layer, in particular in the temporal evolution of the droplet collision/evaporation rates and in their spectrum broadening. These findings were linked to the large intermittency of the small-scale turbulence, which is driven by the anisotropy of the carrier flow shearless layer and by the active scalars transported there.

The aim of the present work is twofold: first, to compute and compare the various microphysical timescales in the cloudy–clear air interfacial layer so far proposed in the literature, second, to infer a possible source term for Twomey's equation (1) that accounts for the

small-scale statistics of the carrier flow at a cloud-top boundary where the updraft is null. We have used the dataset computed from the aforementioned direct numerical simulation campaign performed by Golshan *et al.*<sup>23</sup> We have adopted a high-resolution pseudospectral method that allows us to observe the temporal evolution of the supersaturation fluctuations and the velocity derivative statistics across the horizontal turbulent shearless mixing layer (for the gas phase dynamics, see Tordella and Iovieno<sup>24</sup>).

The physical model of a shearless cloud–clear air interface, together with the relevant governing equations of the direct numerical simulations, is presented in Sec. II. The obtained results are discussed in Sec. III, and the conclusions are drawn in Sec. IV.

## II. PHYSICAL PROBLEM AND MATHEMATICAL FRAMEWORK

### A. Physical model and governing equations

The aim here has been to study the transient decay of a top cloud–clear air interface by performing direct numerical simulations of a turbulent shearless mixing layer. This idealized interfacial layer separates two regions. A warmer, droplet-laden cloud region is located at the bottom half of the domain, and it is rich in water vapor and kinetic energy. A clear air less energetic area lies in the top half of the computational domain, which is a parallelepiped made up of two adjacent cubes, see Fig. 1, panels (a) and (b).

A turbulent layer without mean shear is a reasonable model of turbulence at the boundary between atmospheric clouds and the surrounding undersaturated air. This flow is considered simple because it is free of the complications associated with the production of turbulence due to the mean flow. However, in reality, it is home to dynamic aspects that are not obvious and have not yet been fully described or understood. We briefly list some of them hereafter. To form a shear-free turbulent layer, it is sufficient that two contiguous non-sheared regions with a different integral scale and the same kinetic initial energy interact. This, in time, can generate a shear-free layer that hosts a gradient of kinetic energy.<sup>25</sup> All the shear-free turbulent layers are inhomogeneous, thus anisotropic, and also intermittent at the small scale level. Anisotropy appears in the main diagonal of the velocity fluctuation gradient, which is characterized by a substantial absence of significant off diagonal terms.<sup>24,26</sup> The growth or reduction of the thickness of the layer is controlled to a great extent by the concomitant action of the local kinetic energy and spatial macroscale gradients. If these gradients have opposite signs across the layer, the thickening of the layer decelerates, and vice versa, if the signs are concordant.<sup>27</sup> If the layers are stratified in density, substrates are formed. In the case of stable stratification, the energy collapses below the two formation region levels. Flow transport across the layer is blocked. In the case of unstable stratification, the sublayer hosts an accumulation of energy, and transport is enhanced.<sup>28</sup>

Moreover, it should be noted that for the case where the most energetic portion in addition to the layer (cloud region) hosts both supersaturated water vapor and water droplets, recent results have shown that (i) the small-scale intermittency of the air flow in the mixing layer is highly correlated with the drop collision rate of both the monodisperse and polydisperse drop size distributions, and (ii) a more intense widening of the drop population size spectrum is observed in the interfacial region with respect to what happens inside the homogeneous cloud region. These results have prompted our interest in

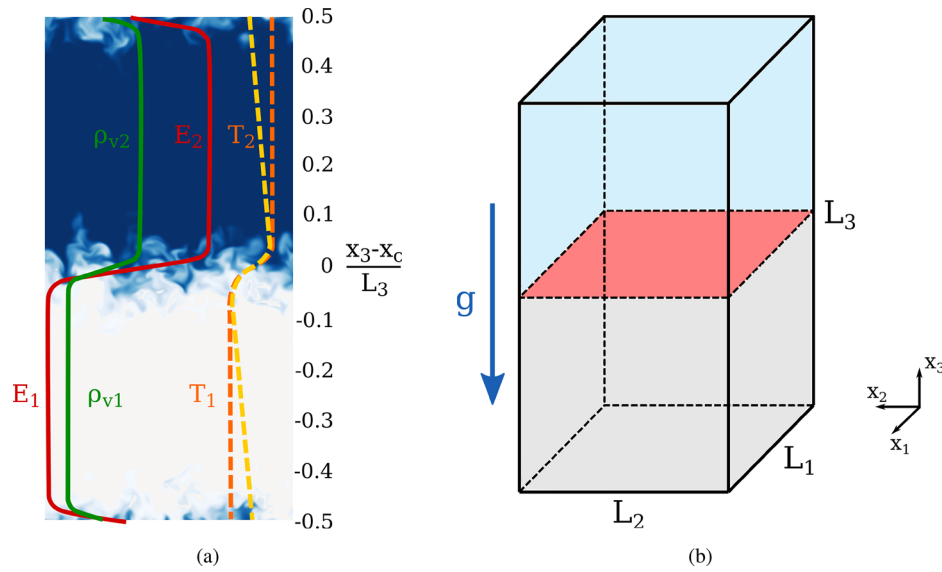


**FIG. 1.** Panel (a): initial distributions of kinetic energy  $E$  (solid dark red line), water vapor density  $\rho_v$  (solid green line), and temperature  $T$  (orange and yellow dash-dotted lines) in the vertical direction across the interfacial mixing layer. The mixing layer is located at  $x_c = L_{12}$  (see Table II). The temperature fluctuation component  $T'(x_3)$  of Eq. (11) is plotted with yellow the dash-dotted line, while the non-periodic physical temperature  $T$  is plotted with the orange dash-dotted line. Subscripts 1 and 2 refer to cloud and clear-air conditions (see Table I). Panel (b): the computational domain is a parallelepiped composed of two adjacent cubes. The total height  $L_3$  is twice  $L_{1,2}$ . Subscripts 1 and 2 refer to the horizontal directions parallel to the mixing layer, whereas subscript 3 indicates the vertical direction.

exploring the correlation between supersaturation fluctuations and the small-scale intermittency of air flow turbulence. A relationship has here been hypothesized to be responsible for the so-called bottleneck problem associated with the interaction of the evaporation–condensation–coalescence processes present in the formation of cumulus rain.

Boussinesq Navier–Stokes equations provide the Eulerian description of the incompressible, stratified, velocity fluctuation,  $u_i$ , along with active scalar transport equations for temperature,  $T$ , and water vapor density  $\rho_v$ <sup>4,17–19,29–31</sup>

$$\frac{\partial u_j}{\partial x_j} = 0, \quad (2a)$$

$$\frac{\partial u_i}{\partial t} + u_j \frac{\partial u_i}{\partial x_j} = -\frac{1}{\rho_0} \frac{\partial p}{\partial x_i} + \nu \frac{\partial^2 u_i}{\partial x_j^2} + \mathcal{B} \delta_{3i}, \quad (2b)$$

$$\frac{\partial T}{\partial t} + u_j \frac{\partial T}{\partial x_j} = \kappa \frac{\partial^2 T}{\partial x_j^2} + \frac{\mathcal{L} C_d}{\rho_0 c_p}, \quad (2c)$$

$$\frac{\partial \rho_v}{\partial t} + u_j \frac{\partial \rho_v}{\partial x_j} = \kappa_v \frac{\partial^2 \rho_v}{\partial x_j^2} - C_d, \quad (2d)$$

where  $\rho_0$  is the Boussinesq density (that is, the mean density of dry air 1000 m above the sea level),  $\nu$  is the kinematic viscosity of the air,  $\kappa$  is the heat diffusivity of the air, and  $\kappa_v$  is the mass diffusivity of the water vapor.  $\mathcal{L}$  is the latent heat of evaporation of the water, and  $c_p$  is the specific heat of the air at the mean domain temperature  $T_0$ . All the physical constants in Eqs. (2a)–(2d) are summarized in Table I. The Boussinesq approximation allows us to take into account small perturbations of a parcel density of moist air due to local temperature and vapor density variations.<sup>32</sup> The buoyancy term,  $\mathcal{B}$ , in Eq. (2b) can be expressed as a function of the local values of  $T$  and  $\rho_v$

$$\mathcal{B} = g \left[ \frac{\Delta T}{T_0} - \frac{\Delta \rho_v}{\rho_0} \left( 1 - \frac{\mathcal{M}_a}{\mathcal{M}_w} \right) \right], \quad (3)$$

where  $\mathcal{M}_a$  and  $\mathcal{M}_w$  are the molar masses of the air and water, respectively. We adopt periodic boundary conditions for the velocity and water vapor density fields in the three directions. The temperature field is non-periodic in the vertical direction and results from the superposition of a triply periodic scalar field and a constant, negative, vertical temperature gradient. The temperature of the cloud region being higher than the clear-air one, the interfacial mixing layer is subject to an unstable stratification with a squared Froude number,  $Fr_{int}^2$ , approximately equal to  $-7$ . This leads to a local increase in the momentum and kinetic energy, as a result of the Boussinesq body-force term in Eq. (2b).

The condensation term  $C_d = C_d(x_i, t)$  in the energy and vapor density equation expresses the water vapor mass absorption (depletion) rate at the surface of all the spherical droplets contained in the cubic computational cell of volume  $(\Delta)^3$ , Vaillancourt *et al.*<sup>29</sup> Since cloud droplets are advected by the turbulent flow,  $C_d$  must be determined in the Lagrangian reference frame used for the liquid water mixing ratio, which is described below in Sec. II B. However, in order to use  $C_d$  in Eqs. (2c) and (2d), it should be represented in the Eulerian frame of reference. The condensation rate field is determined as

$$C_d = \frac{1}{\Delta x^3} \frac{dm_w}{dt} = \frac{4\pi\rho_w}{\Delta x^3} \sum_{j=1}^{N_\Delta} R_j^2(X_j(t)) \frac{dR_j(X_j(t))}{dt}, \quad (4)$$

where  $R_j(t)$  and  $X_j(t)$  are the radius and the coordinate of the  $j$ th drop contained within the grid cell, respectively, and  $N_\Delta$  represents the number of drops inside each grid cell. The interpolation of Eulerian field values at grid points to the positions occupied by the water droplets inside the cell is obtained via second-order Lagrange



**TABLE I.** The key physical parameters used in the numerical experiments.

| Quantity   | Symbol          | Value                 | Unit                             |
|--|-----------------|-----------------------|----------------------------------|
| Latent heat of evaporation   | $\mathcal{L}$   | $2.48 \times 10^6$    | $\text{J kg}^{-1}$               |
| Heat capacity of the air at a constant pressure  | $c_p$           | 1005                  | $\text{J kg}^{-1} \text{K}^{-1}$ |
| Gravitational acceleration   | $g$             | 9.81                  | $\text{m/s}^2$                   |
| Molar mass of the water  | $\mathcal{M}_w$ | 18                    | $\text{kg l mol}^{-1}$           |
| Gas constant of the water vapor  | $R_v$           | 461.5                 | $\text{J kg}^{-1} \text{K}^{-1}$ |
| Molar mass of the dry air  | $\mathcal{M}_a$ | 29                    | $\text{kg l mol}^{-1}$           |
| Gas constant of the air  | $R_a$           | 286.7                 | $\text{J kg}^{-1} \text{K}^{-1}$ |
| Diffusivity of the water vapor mass  | $\kappa_v$      | $2.52 \times 10^{-5}$ | $\text{m}^2/\text{s}$            |
| Thermal conductivity of the dry air  | $K$             | $2.5 \times 10^{-2}$  | $\text{W m}^{-1} \text{K}^{-1}$  |
| Liquid water density   | $\rho_w$        | 1000                  | $\text{kg/m}^3$                  |
| Dry air density at an altitude of 1000 m   | $\rho_0$        | 1.11                  | $\text{kg}^3$                    |
| Dry air kinematic viscosity  | $\nu$           | $1.5 \times 10^{-5}$  | $\text{m}^2/\text{s}$            |
| Average temperature of the whole domain  | $T_0$           | 281.16                | K                                |
| Average temperature of the cloud region  | $T_1$           | 282.16                | K                                |
| Average temperature of the clear air region  | $T_2$           | 280.16                | K                                |
| Background temperature gradient (unstable)   | $G$             | $-2/1.024$            | $\text{K m}^{-1}$                |
| Brunt–Väisälä amplification factor   | $\mathcal{N}^2$ | $-0.69$               | $\text{s}^{-2}$                  |
| Droplet growth coefficient   | $K_s$           | $8.6 \times 10^{-11}$ | $\text{m}^2/\text{s}$            |
| Accumulation mode (radius)   | $r_d$           | 0.01                  | $\mu\text{m}$                    |
| Kelvin coefficient   | $A$             | $1.15 \times 10^{-9}$ | m                                |
| Raoult solubility parameter for inorganic, hygroscopic substances such as ammonium sulfate, lithium chloride, etc. | $B$             | 0.7                   | ...                              |
| Initial relative humidity in the cloud region  | $RH_1$          | 1.02                  | ...                              |
| Initial relative humidity in the clear air region  | $RH_2$          | 0.7                   | ...                              |
| Initial liquid water content   | $LWC_0$         | $7.9 \times 10^{-4}$  | $\text{kg/m}^3$                  |

polynomials. An inverse procedure is used to calculate the condensation rate, which is determined at the first step at each droplet position and then relocated to the closest of the eight grid vertices. The time derivative,  $dR_j/dt$ , expresses the droplet condensational shrinkage (growth) rate, as defined in Eq. (8).

## B. Lagrangian droplet dynamics and droplet populations

The Lagrangian motion of each  $k$ th droplet in the physical system is modeled by a tracker of the type<sup>29,33</sup>

$$\frac{dX_{ki}}{dt} = V_{ki}, \quad (5a)$$

$$\frac{dV_{ki}}{dt} = \frac{1}{\tau_k} [u_i(X_{ki}, t) - V_{ki}] + g\delta_{i3} \left(1 - \frac{\rho_0}{\rho_w}\right), \quad (5b)$$

which features two vector equations for position,  $X_{ki}$ , and velocity,  $V_{ki}$ , of a droplet within the reference frame, where  $i$  indicates the direction. The momentum equation is derived for low-Reynolds spherical droplets<sup>29,31</sup> and only accounts for the contribution of Stokes' drag and gravity, while the effects of Faxen and Basset's history force are negligible.<sup>23,31,34</sup> The inertia of a spherical droplet is proportional to its surface and is often expressed through a characteristic timescale, that is, the droplet response time ( $\tau_d$ ) of the  $k$ th droplet with radius  $R_k$ <sup>10</sup>

$$\tau_{dk} = \frac{2\rho_w R_k^2}{9\rho_0 \nu}, \quad (6)$$

which is also the time constant of the solution to Eq. (5b) for a steady, homogeneous flow.

It should be noted that, in a similar way to what is done for the condensation rate field, Eulerian flow field quantities have to be determined at the droplet position to numerically proceed with Lagrangian equations. In this context, we adopted a simplified feedback on the droplet flow. The direct effect of the liquid droplet drag on the velocity field is neglected in the buoyancy term in the momentum equation. The feedback is, therefore, indirect and is confined to the coupling of the temperature field with the velocity field and the vapor mixing ratio through the condensation rate. The rationale behind this position depends on the smallness Stokes' numbers of the drops and liquid mass and volume fractions  $\sim 10^{-3}$  and  $\sim 10^{-6}$ , respectively. In fact, for radii in the range  $[1-30] \mu\text{m}$ , the initial transient values of Stokes' numbers are in  $[0.02-0.7]$ , while the end of transient values are in  $[0.002-0.066]$ , which means Reynolds numbers of the drops much lower than 1.

Spherical cloud droplets are assumed to collide and coalesce with full collision and coalescence efficiency whenever their relative distance falls below the sum of the respective radii

$$\left[ \sum_{i=1}^3 (X_{li} - X_{ki})^2 \right]^{1/2} \leq R_l + R_k.$$

The single droplet resulting from coalescence conserves the total mass and momentum of the colliding drops. In present work, we have focused on the effects associated with anisotropy and intermittency of the interfacial layer separating the cloud region from the clear-air ambient. According to a hypothesis that is commonly adopted in the literature,<sup>35,36</sup> dynamic and kinematical collision kernels are very similar and the collision efficiency is close to unity (see, for instance, Wang *et al.*,<sup>36</sup> Tables 2–4). Therefore, we did not consider the parametrization on the efficiency as a first order effect in the present study.

Both monodisperse and polydisperse droplet size distributions are considered in the present simulation campaign (Fig. 2). At the beginning of the simulation, the droplets are randomly distributed in the cloud region of the computational domain, where the clear air region is initially void. The number of droplets,  $N_{\text{tot-mono}} = 8 \times 10^6$ , for the monodisperse population, is determined from the typical liquid water content  $LWC_0 \sim 0.8 \text{ g/m}^3$  encountered in warm cumulus clouds and the chosen initial monodisperse radius,  $R_{0,\text{mono}} = 15 \mu\text{m}$ ,

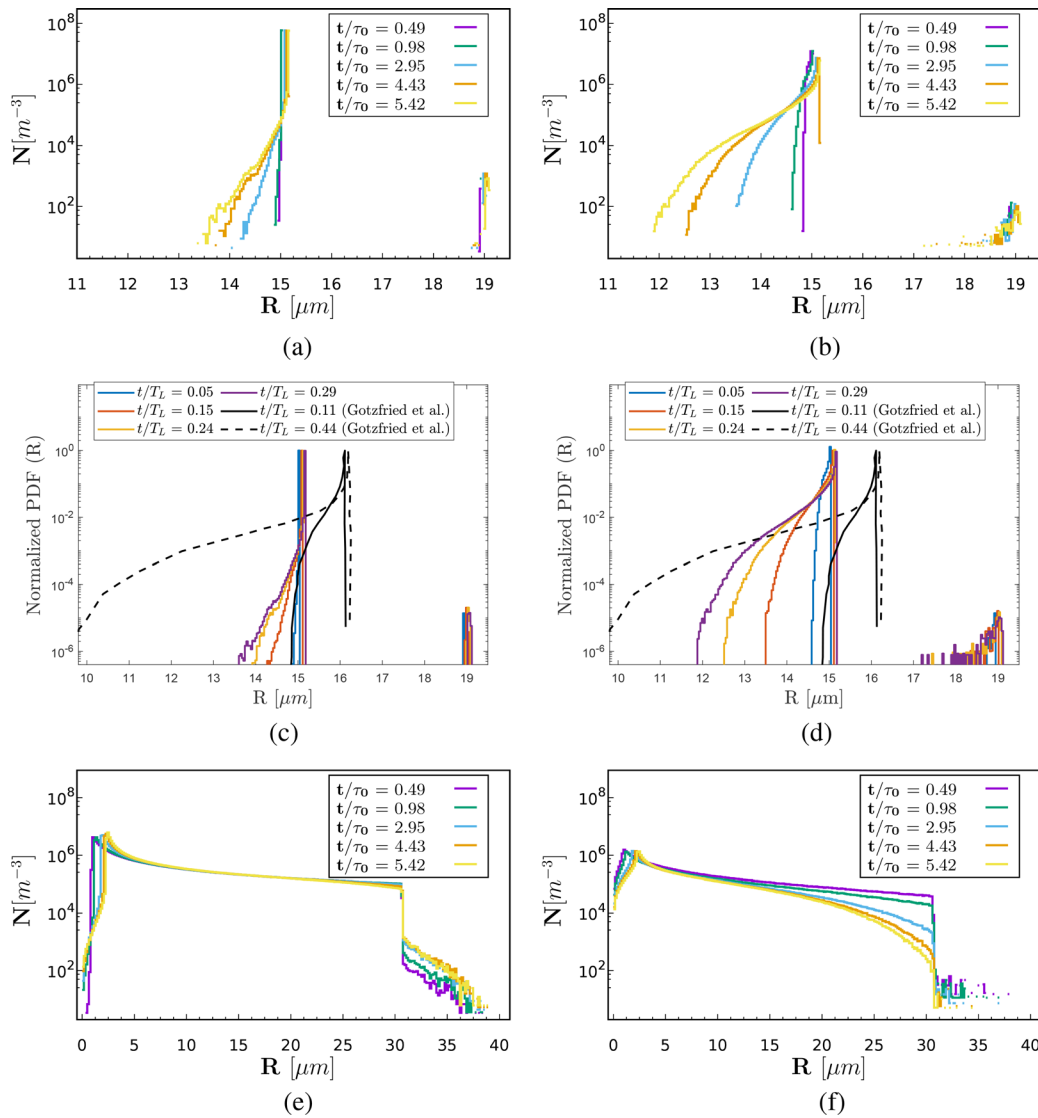


**FIG. 2.** Droplet size distributions as a function of the radius classes. Panels (a) and (b): size distribution for a monodisperse population ( $R = 15 \mu\text{m}$ ) in the cloud and interface regions, respectively. Comparison of normalized PDF (probability density function) values of droplet radii at different time instances. In panels (c) and (d), the present results (color lines) are compared with the results by Götzfried *et al.*<sup>31</sup> (solid/dashed black lines), which were computed over the entire domain, including the homogeneous cloud, the interface layer and the clear-air homogeneous region. It should be noted that the simulation made by Götzfried *et al.* does not include any collisions, which caused the second peak on the right in the distributions. PDF values of both datasets are normalized with the peak value. Results are plotted for non-dimensional large eddy turnover time. Panels (e) and (f): size distribution for a polydisperse (equal mass in the droplet volume classes,  $R \in [0.6-30] \mu\text{m}$ ) population in the cloud and interface regions, respectively. (a) Monodisperse, cloud; (b) monodisperse, interface; (c) comparison, cloud; (d) comparison, interface; (e) polydisperse, cloud; and (f) polydisperse, interface.

$$N_{\text{tot-mono}} = LWC_0 \frac{4}{3} \pi \rho_w R_{0,\text{mono}}^3. \quad (7)$$

The faster dynamics of the droplet spectrum inside the highly intermittent mixing layer, with respect to that shown in the nearly Gaussian cloud turbulence, should be noted. Panels (a) and (b) in Fig. 2 highlight the intense acceleration of the broadening of the droplet spectrum in the interfacial layer [standard deviation time variation:  $0.015(t/\tau_0) + 0.05$  in the cloud and  $0.23(t/\tau_0) + 0.003$  in the mixing, see Figs. 7 and 11 and Table 3 in Golshan *et al.*<sup>23</sup> Panels (c)

and (d) in Fig. 2] show, for an initially flat polydisperse size distribution, a faster rate of modification toward the typical peaky shape in the interface than in the cloudy region. In fact, the temporal narrowing of the standard deviation goes like  $-0.19(t/\tau_0) + 19.7$  in the cloud and as  $-0.74(t/\tau_0) + 17.94$  in the mixing, see Figs. 8 and 12 and Table 3 in Golshan *et al.*<sup>23</sup>

Götzfried *et al.*<sup>31</sup> conducted a similar numerical experiment in which they studied the response of an ensemble of cloud water droplets to the turbulent entrainment of clear air in a cloud filament.

They presented three simulations of a monodisperse droplet population, where the droplet size distributions evolved mainly due to condensation–evaporation processes. However, they did not include any collision–coalescence processes in their simulations, and they only considered monodisperse size distributions. Figures 2(c) and 2(d) show a good agreement with simulation made by Götzfried *et al.* apart from the second peak due to collision–coalescence. In both cases, the size distributions broaden to the left as a result of the evaporation process, starting from the initial radius. There is still a negligible enhancement of the size distribution during transient on the right side in both studies.

Broad droplet size distributions have been observed in both *in situ* measurements of forming shallow cumulus clouds<sup>15</sup> and in laboratory experiments.<sup>14</sup> These distributions usually show a peak for relatively small radii (1–10  $\mu\text{m}$ ), which is accompanied by a monotonical decrease in concentration as the radius increases. However, the existence of a general and ubiquitous functional shape of the droplet size distribution in shallow cumulus clouds is still a matter of debate.<sup>37</sup> Without any claim of generality, we introduce an initial polydisperse distribution in which the same mass is allocated to each class of radii. Each volume class gathers droplets that have roughly the same volume.<sup>23</sup>

A droplet is subject to ambient supersaturation, which is obtained through a polynomial interpolation with the neighboring cell values. The condensation–evaporation rate of the spherical  $k$ th droplet can be estimated according to<sup>6,12,38</sup>

$$\frac{dR_k}{dt} = \frac{K_s}{R_k} \left( S - \frac{A}{R_k} + \frac{Br_d^3}{R_k^3} \right), \quad (8)$$

where  $S$  is the supersaturation or saturation deficit (see Sec. II D),  $A$  is the Kelvin coefficient,  $B$  is the hygroscopicity parameter,  $R_k$  is the  $k$ th droplet radius, and  $r_d$  is the accumulation radius. The second and the third terms on the right-hand side are known as the Kelvin and Raoult terms, respectively. The Kelvin term describes the effect of droplet curvature and surface tension, while the Raoult term indicates aerosol hygroscopicity. The diffusion coefficient  $K_s$  is slightly sensitive to local equilibrium thermodynamics.<sup>7,38,39</sup> It includes the self-limiting effects of latent heat release. This diffusion coefficient is considered to be constant in the literature, for typical warm cloud conditions, where the characteristic heat flux due to latent heat from a small variation in the droplet temperature is of the same order as the heat flux due to thermal conduction for the same temperature difference. The temperature dependence of this constant is weak [the  $K_s$  value in  $\text{m}^2 \text{s}^{-1}$  ranges from  $5.07 \times 10^{-11}$  at  $T = 270 \text{ K}$ , to  $1.17 \times 10^{-10}$  at  $T = 293 \text{ K}$  (Refs. 17 and 40)]. In agreement with our volume averaged initial temperature of 281 K, we used the value  $8.6 \times 10^{-11} \text{ m}^2 \text{s}^{-1}$ . The interpolation of Eulerian field values at grid points to the position occupied by the water droplets inside the cell is obtained via second-order Lagrange polynomials. An inverse procedure is then used for the calculation of the condensation rate, which is determined at the first step at each droplet position and then relocated to the closest of the eight grid vertices. A collision is hypothesized to occur when the distance between the centers is equal to or less than the sum of their radii. Such collisions are assumed to be completely inelastic.

Supersaturation

$$S(\mathbf{x}, t) = \frac{\rho_v(\mathbf{x}, t)}{\rho_{vs}(T)} - 1 = RH - 1$$

is defined as the ratio between the water vapor and the saturated vapor densities (i.e., the relative humidity)  $-1$ . The relative humidity  $RH = \rho_v/\rho_{sv}$  and supersaturation (or saturation deficit) are functions of the saturated vapor density,  $\rho_{vs}$ , whose dependence on temperature is described by the Clausius–Clapeyron equation<sup>7</sup>

$$\frac{d\rho_{vs}}{\rho_{vs}} = \left( \frac{\mathcal{L}}{R_v T} - 1 \right) \frac{dT}{T}, \quad (9)$$

where  $\mathcal{L}$  is the latent heat of evaporation (condensation) and  $R_v$  is the gas constant of the water vapor. It is hypothesized that the droplet–gas interphase coupling is negligible,<sup>41</sup> and the droplet motion, therefore, does not exert any relevant dynamical effect on the carrier field. Conversely, the turbulent field affects the motion of the water drops to a great extent. Phase transition at the droplet surface results in the exchange of water vapor and latent heat between the two phases, thus perturbing the buoyancy term in momentum Eq. (2b).

Since the coefficients  $A$ ,  $B$ , and  $r_d$  are hypothesized to be constant, the droplet growth rate mainly depends on the local value of  $S$  and on the droplet radius  $R$ . The droplet growth (shrinkage) rate (8) is plotted in Fig. 3 for three constant values of supersaturation  $S$ , where the competing effects of the Kelvin and Raoult terms can be appreciated by observing the orange curve, which describes a saturated environment. In the present conditions, the Kelvin effect becomes important for  $R < 1 \mu\text{m}$ , and it is soon outweighed by the Raoult effect as the droplet (aerosol) radius falls below  $\approx 23 \text{ nm}$ . The Raoult term is the term that is prevalent below this threshold.

### C. Numerical experiment setup and DNS algorithm

The parallelepiped-shaped domain (see Fig. 1) is made up of two adjacent cubes of  $512^3$  cells each. Two initial zero-mean,

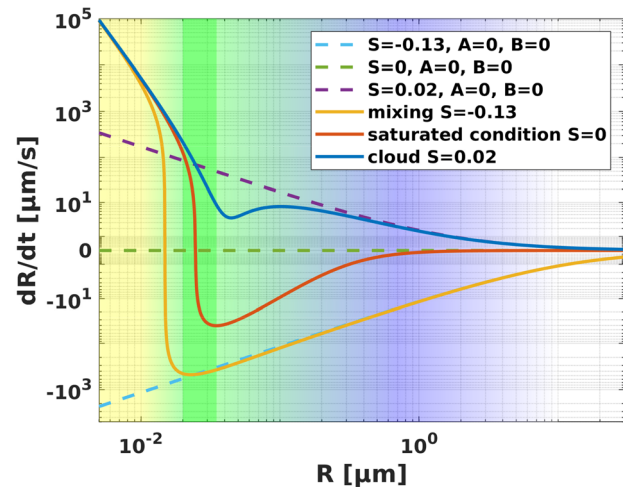


FIG. 3. The plot shows the condensational growth rate [Eq. (8)] for a drop of given radius  $R$  for supersaturated ( $S = 0.02$ , as in the cloud region of the present work), saturated ( $S = 0$ ), and subsaturated ( $S = -0.3$ ) conditions. The contributions due to the effect of both surface tension (Kelvin) and curvature (Raoult) are negligible for droplets of radius above  $1 \mu\text{m}$ , such as the ones considered in the present work. The dashed lines only represent the effect of supersaturation, when the Kelvin and Raoult terms are set equal to zero. The vertical green bar highlights the range of radii below above which the Raoult and Kelvin terms dominate, respectively.



homogeneous, isotropic air fluctuation fields are generated inside the two cubes. The turbulent spectra show the same functional shape and, hence, the same integral scale. The cube in the lower half of the parallelepiped—which from now on is referred to as the cloud region—initially hosts a higher turbulent kinetic energy,  $E$ , and dissipation (decay) rate,  $\varepsilon$ , than the upper cube, which models a clear air region, see Figs. 1(b) and 4, panels (a) and (b). The initial integral scale is set equal in the two regions so as not to introduce a further control parameter—the integral length gradient across the layer—on the interface evolution and the related transport dynamics.<sup>25,27</sup> The summary of simulation parameters is given in Table II.

The root mean square velocity in the more energetic region is  $u_{rms} \cong 0.11 \text{ ms}^{-1}$ , which represents the large-scale energy in the cumulus spectral subrange of wavelengths 0.002 to 0.25 m. Since our system is time decaying, the initial dissipation rate was purposely set high in order to reach the commonly values observed in cumulus clouds in the central part of the transient. However, the initial dissipation rate  $\varepsilon \sim 500 \text{ cm}^2/\text{s}^3$  is of the same order as those measured by

MacPherson and Isaac<sup>42</sup> in cumulus clouds in the proximity of the top (cloud # 1 measurement, 100 m below the cloud top, height of the top 4800 m) although in the presence of a much higher kinetic energy of the air fluctuation ( $rms \sim 2 \text{ m/s}$ ). Lower values ( $10 \sim 20 \text{ cm}^2/\text{s}^3$ ) have been reported,<sup>43–46</sup> and they are obtained during the transient decay, see Fig. 4, panels (c) and (d). The estimated Kolmogorov scale is  $\eta_0 \cong 0.5 \text{ mm}$ , and the highest resolved wavenumber is  $k_{max} = \pi/\Delta x = \pi \times 10^3 \text{ m}^{-1}$ .<sup>47</sup> Since we have  $k_{max}\eta_1 \cong 1.6$ , the resolution is acceptable for the problem at hand.<sup>33,48</sup>

The DNS algorithm is based on the dealiased pseudospectral Navier–Stokes solver described in Ref. 49. Code versions and releases are available on the official website of Philofluid Research Group. This software has been used in several works conducted by the group<sup>23,24,26–28,50</sup> to investigate turbulence self-diffusion in shearless mixings, with passive or active scalars, and water drop populations. Spectral discretization is achieved by means of the Fourier–Galerkin method with pseudo-spectral treatment of the advection terms in the momentum (2b) equation, and scalar transport ones (2d) and (2c).

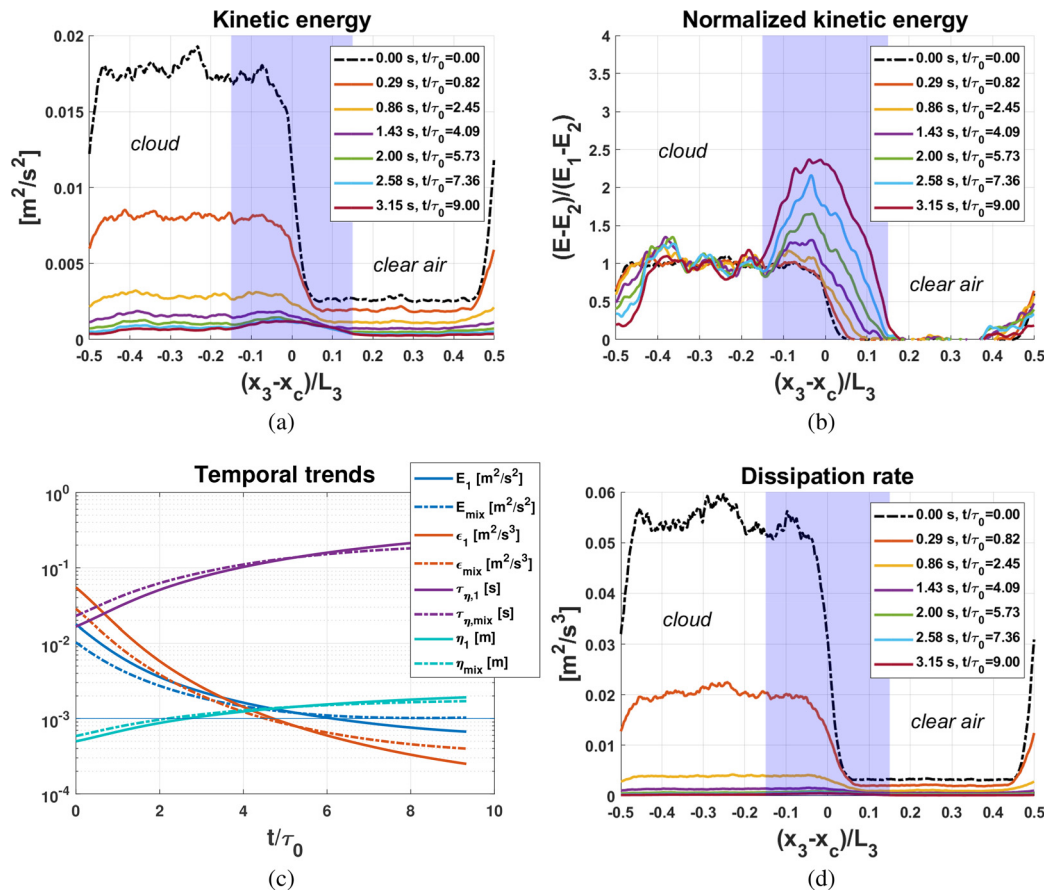


**FIG. 4.** Trends of the kinetic energy and turbulent dissipation rate. (a) Evolution of the turbulent kinetic energy  $E$  across the domain for an initial unstable background temperature gradient. The interface is located at the center of the figure (that is, for  $x_3 \cong x_c$ ). Mildly unstable stratification ( $Fr_{int}^2 \cong -7$ ). (b) Normalized values of  $E(t)$  with respect to the mean kinetic energy in the cloud  $E_1(t)$  and clear air  $E_2(t)$  regions. The initial energy ratio across the interface is  $E_1/E_2 = 6.7$ . The plotted values of  $E$  are the planar averages of each horizontal plane. (c) Transient evolution of the kinetic energy  $E$ , the dissipation rate  $\epsilon$ , the Kolmogorov timescale  $\tau_{\eta}$ , and the Kolmogorov length scale  $\eta$  in the cloud and mixing regions (subscripts 1 and 2, respectively). The thin horizontal line indicates the grid width,  $\Delta x$ , in meters. (d) Evolution of the dissipation rate  $\epsilon$  across the domain.

**TABLE II.** The key simulation parameters and initial conditions, which are the same for all the runs.

| Quantity   | Symbol                                      | Value                                       | Unit                    |
|--|---|---|-------------------------|
| Domain size  | $L_{1,2}^2 \cdot L_3$                       | $0.512^2 \times 1.024$                      | $\text{m}^3$            |
| Domain discretization  | $n_{1,2}^2 \cdot n_3$                       | $512^2 \times 1024$                         | ...                     |
| Grid step  | $\Delta x$                                  | $10^{-3}$                                   | m                       |
| Initial rms velocity (cloud)   | $u_{rms,1}$                                 | 0.11  | $\text{m s}^{-1}$       |
| Initial integral scale   | $\ell_0$                                    | $2.65 \times 10^{-2}$                       | m                       |
| Initial dissipation rate (cloud)   | $\varepsilon_1$                             | 0.05  | $\text{m}^2/\text{s}^3$ |
| Initial energy ratio (cloud–clear air)                                     | $E_1/E_2 = u_{rms,1}^2/u_{rms,2}^2$         | 6.7   | ...                     |
| Initial Kolmogorov time (cloud)  | $\tau_{\eta 0} = (\nu/\varepsilon_1)^{1/2}$ | $1.74 \times 10^{-2}$                       | s                       |
| Initial Kolmogorov length scale (cloud)                                    | $\eta_0 = (\nu^3/\varepsilon_1)^{1/4}$      | $5.1 \times 10^{-4}$                        | m                       |
| Initial eddy turnover time   | $\tau_0 = 2\ell/(u_{rms,1} + u_{rms,2})$    | 0.35  | s                       |
| Initial Reynolds number (cloud)  | $\text{Re}_\ell = u_{rms}\ell/\nu$          | 196   | ...                     |
| Droplet response time ( $1\text{ }\mu\text{m}$ , $30\text{ }\mu\text{m}$ ) | $\tau_d = 2\rho_v R/(9\rho_0\nu)$           | $4.4 \times 10^{-4}$ , $1.3 \times 10^{-2}$ | s                       |
| Initial droplet Stokes numbers ( $R \in 1 - 30\text{ }\mu\text{m}$ )       | $St = \tau_d/\tau_{\eta 0}$                 | 0.025–0.7                                   |                         |
| Final droplet Stokes number ( $R \in 1 - 30\text{ }\mu\text{m}$ )          | $St = \tau_d/\tau_{\eta f}$                 | 0.002–0.066                                 |                         |
| Initial Taylor microscale Reynolds number                                  | $\text{Re}_\lambda = u_{rms}\lambda/\nu$    | 52  | ...                     |
| Integration time step  | $\Delta t = 1/20 \cdot \Delta x/u_{rms}$    | $4.64 \times 10^{-4}$                       | s                       |
| Initial number of droplets (monodisperse distribution)                     | $N_{tot-mono}$                              | $8 \times 10^6$                             | ...                     |
| Initial number of droplets (polydisperse distribution)                     | $N_{tot-poly}$                              | $10^7$                                      | ...                     |
| Initial droplet radius (monodisperse distribution)                         | $r_{0,mono}$                                | 15  | $\mu\text{m}$           |
| Initial droplet radius (polydisperse distribution)                         | $r_{0,poly}$                                | 0.6–30                                      | $\mu\text{m}$           |

Time integration is performed, according to Ireland,<sup>33</sup> with a second-order explicit Runge–Kutta method.<sup>51</sup> The diffusive terms for the momentum, internal energy (2c), and vapor density fields (2d) are computed by means of exponential integration. Droplet velocities (5a) and accelerations (5b) are integrated with a second-order explicit method and a second-order implicit trapezoidal method, respectively. The implicit structure of the integration scheme used for Eq. 5(b) ensures numerical stability for arbitrary values of  $\Delta t$ .

The code stores the velocity, temperature, and vapor fields in three-dimensional arrays and distributes them along one direction in both physical and Fourier spaces. The three-dimensional discrete Fourier transform is performed with the FFTW library. A slab-like parallelization is implemented with Message Passage Interface (MPI) standard libraries.

#### D. Initial and boundary conditions for the flow velocity, temperature, and vapor fields

Two homogeneous isotropic solenoidal turbulent fields, with zero-mean velocity and different kinetic energies, that mix at a common interface, are studied in this numerical experiment. A smoothing function,  $p(x_3)$ , is applied to modulate the velocity and scalar vapor fields along  $x_3$ .<sup>27,28</sup>

$$\begin{aligned}
 u_i(x_j) &= u_{i1}(x_j)p(x_3) + u_{i2}(x_j)\sqrt{1-p^2(x_3)}, \\
 \rho_v &= \rho_{v1}p(x_3) + \rho_{v2}\sqrt{1-p^2(x_3)}, \\
 p(x_3) &= 1 + \tanh\left[a\frac{x_3}{L_3}\right] \tanh\left[a\left(\frac{x_3}{L_3} - \frac{1}{2}\right)\right] \tanh\left[a\left(\frac{x_3}{L_3} - 1\right)\right],
 \end{aligned}$$

where  $\rho_{v1} = \rho_{vs}(T_1)RH_1$  and  $\rho_{v2} = \rho_{vs}(T_2)RH_2$  were chosen to obtain the desired level of supersaturation in both regions (see Table I). Direction  $x_3$  is the inhomogeneous direction and  $L_3$  is the width of the computational domain in the  $x_3$  direction. Constant  $a$  determines the initial mixing layer thickness  $\Delta$ , which is conventionally defined as the distance between the points with normalized energy values of 0.25 and 0.75, whenever the low energy side is mapped to zero and the high energy side to one. When  $a = 12\pi$ , the initial  $\Delta/L_3$  ratio is about 0.026, a value that was chosen so that the initial thickness would be large enough to be resolved but small enough to have large regions of homogeneous turbulence during the simulations.

The initial distributions of the velocity, temperature, and water vapor density fields in the vertical direction are plotted in Fig. 1(a).

The same initial values of  $T$  and  $\rho_v$  are defined for all the cells of a horizontal plane and are, thus, functions of their vertical position with respect to the interface. As in Refs. 23 and 50, the vapor field is periodic and continuous in the three directions, whereas the temperature field

$$T(x_3, 0) = T'(x_3, 0) + T_0 + G\frac{x_3}{L_3} \quad (10)$$

is composed of the sum of a vertical, triple-periodic fluctuating temperature  $T'(x_3, t)$ , a static component  $Gx_3$ , and a global average temperature  $T_0$ . The periodic term  $T'$  in Eq. (10) is defined with a hyperbolic tangent

$$T'(x_3, 0) = \frac{T_2 - T_1}{2} \cdot \left[ \tanh\left(a\left(\frac{x_3}{L_3} - \frac{1}{2}\right)\right) - \frac{2x_3}{L_3} + 1 \right]. \quad (11)$$

However, the code is required to solve the periodic field  $T'$ . Equation (2c) then becomes

$$\frac{\partial T'}{\partial t} + u_1 \frac{\partial T'}{\partial x_1} + u_2 \frac{\partial T'}{\partial x_2} + u_3 \frac{\partial (T' + Gx_3)}{\partial x_3} = \kappa \nabla^2 T' + \frac{\mathcal{L}C_d}{\rho_0 c_p}.$$

The cloud–clear air interface is located in the center  $(x_3 - x_c)/L_3 \cong 0$ , with  $x_c = L_{12}$ . We define the distance between the points whose normalized temperature  $(T - T_{min})/(T_{max} - T_{min})$  is 0.75 and 0.25, respectively, as the width of mixing layer region  $\Delta$ .<sup>24,27,52</sup> The squared Brunt–Väisälä frequency,  $\mathcal{N}^2 = g \frac{\delta T}{T_0} \frac{1}{\Delta} \cong -0.69 \text{ Hz}^2$ , is negative and, thus, describes an unstable environment. The internal Froude number associated with this stratification is initially

$$\text{Fr}_{int}^2 = \frac{u_{rms,av}^2}{\mathcal{N}^2 \Delta^2} \cong -7.$$

The saturated vapor density, the relative humidity, and the supersaturation are computed with the values of  $T$  expressed by Eq. (10).

### III. RESULTS: VELOCITY AND SUPERSATURATION FLUCTUATIONS, AND TURBULENCE BROADENING OF THE DROPLET SIZE DISTRIBUTION

Droplet and flow statistics are taken from horizontal  $x_1 - x_2$  planes at a constant  $x_3$  and plotted with respect to the normalized height  $(x_3 - x_c)/L_3$ , with  $x_c$  being the position of the cloud–clear air interface, and  $L_3 = 2L_{1,2}$  being twice the length of the edge of the cube. To observe the interface cloud–clear air dynamics, it is necessary to focus on the evolution of the statistics along the non-homogeneous (vertical) direction of the domain. The mean, standard deviation, and higher order-moments are computed over the cells in the same horizontal plane and associated with the corresponding vertical coordinate  $x_3$ . The covariance for each horizontal plane

$$\text{cov}_{X,Y}(x_3, t) = \frac{1}{n_1 n_2} \sum_{i,j=1}^{n_1, n_2} (X(x_1, x_2; x_3, t) - \bar{X})(Y(x_1, x_2; x_3, t) - \bar{Y}), \quad (12)$$

where the over-line indicates the average of a given physical quantity in the  $x_1, x_2$  planes and

$$\bar{X}(x_3, t) = \frac{1}{n_1 n_2} \sum_{i,j=1}^{n_1, n_2} X(x_1, x_2; x_3, t). \quad (13)$$

The Pearson product–moment correlation coefficient of two planar averaged quantities,  $\bar{X}(t)$  and  $\bar{Y}(t)$ , only depends on the time and when used to correlate variations across the interface layer  $\Delta(t)$ , it can be written as

$$\rho_{X,Y_\Delta(t)} = \sum_{k=1}^{n_\Delta} \frac{(\bar{X}(x_3, t) - \bar{X}_\Delta(t))}{\sigma_{\bar{X}}} \frac{(\bar{Y}(x_3, t) - \bar{Y}_\Delta(t))}{\sigma_{\bar{Y}}}, \quad (14)$$

where subscript  $\Delta$  stands for the quantity averaged inside the interface and  $n_\Delta$  is the number of planes inside the interface.

The kinetic energy inside the homogeneous cloudy and clear air regions, decays over time with a power-law exponent (see Fig. 4) of the  $E/E_0 \sim (t/\tau_0)^{-n}$  type, where  $n$  ranges from 1.6 to 2.15.<sup>27,53</sup> The initial values of the root mean square velocity of the flow, of the longitudinal integral length scale, and of the eddy turnover time

are reported in Table II. The eddy turnover time  $\tau_0 = 2\ell_0/(u_{rms,c0} + u_{rms,a0})$  is computed from the initial integral length scale and root mean square velocity of the flow, averaged over the domain, and has an initial value of 0.35 s.

The decay of both kinetic energy  $E$  and dissipation rate  $\varepsilon$  can be observed in Fig. 4. During the decay, the integral scale grows homogeneously over the entire domain.

The system relaxes to a quasi-steady-state condition as values of  $\varepsilon$  of the order of  $10 \text{ cm}^2/\text{s}^3$  are reached inside the mixing layer. Values of this order of magnitude have already been measured in shallow cumulus clouds.<sup>10,43</sup>

The average value of  $E$  quickly decreases during the transient. However, the effects of the unstable stratification are highlighted by the normalized kinetic energy,  $(E - E_2)/(E_1 - E_2)$ , which in fact shows a hump that amplifies in time [see Fig. 4(b), and Figs. 11 and 12 in Gallana *et al.*<sup>28</sup>]. The warmer air close to the interface is convected upward and gains vertical velocity, thus increasing the kinetic energy locally. This injection of kinetic energy at the small scales of the turbulence affects the mixing process by enhancing the vertical advection of the dispersed water droplets, water vapor, and internal energy up to the subsaturated region. High values of higher moments of the spatial longitudinal derivatives of the velocity indicate the high anisotropy and intermittency of the small-scale of the carrier flow in the mixing region. Small-scale intermittency in the mixing region is associated with accelerated droplet population dynamics and an increased collision–coalescence rate, see Fig. 2 in Sec. II and also Table III and Figs. 11 and 12 in Golshan *et al.*<sup>23</sup> The time required by the two populations to reach the same width for the evaporation and condensation processes is estimated by equating the time variations of the standard deviations of the monodisperse and polydisperse size distributions. The estimate is about  $100\tau_0$  in the cloudy region, which is homogeneous and isotropic. The estimate is about  $18, 5\tau_0$  in the interface region, i.e., more than five times faster. A remarkable acceleration of the broadening of the droplet size distribution, due to turbulent fluctuations, is, therefore, observed in the shear-free mixing layer that separates the cloud from the sub-saturated environmental air.

Planar averages and higher order statistical moments of supersaturation across the cloudy–undersaturated ambient air interface layer are shown in Fig. 5. The high intermittency of the distributions should be noted. Very high values of both skewness and kurtosis are reached on the two sides of the mixing layer. Moreover, comparatively higher absolute values can be observed at the border with the cloudy region (S down to  $-8$ , K up to  $60$ ), where the vapor flux is spatially increasing, with respect to that observed at the border with sub-saturated air (S up to  $4$ , K up to  $20$ ), where the vapor flux is spatially decreasing.<sup>28</sup>

The droplet statistics have been computed over the horizontal planes to complement the data in Fig. 2. From now on, we denote the droplet numerical concentration with the symbol  $N$ . The results of the monodisperse and polydisperse distributions across the mixing layer are shown in Fig. 6, where both the droplet radius and the concentration are plotted along  $x_3$ . At the beginning of the transient, the droplets populate the lower part of the domain and are randomly distributed within the cloud. The core environment of the cloud is supersaturated [see Fig. 5(a)], and this permits a uniform condensation growth of the droplets to take place within the cloud. As the central mixing proceeds, a few

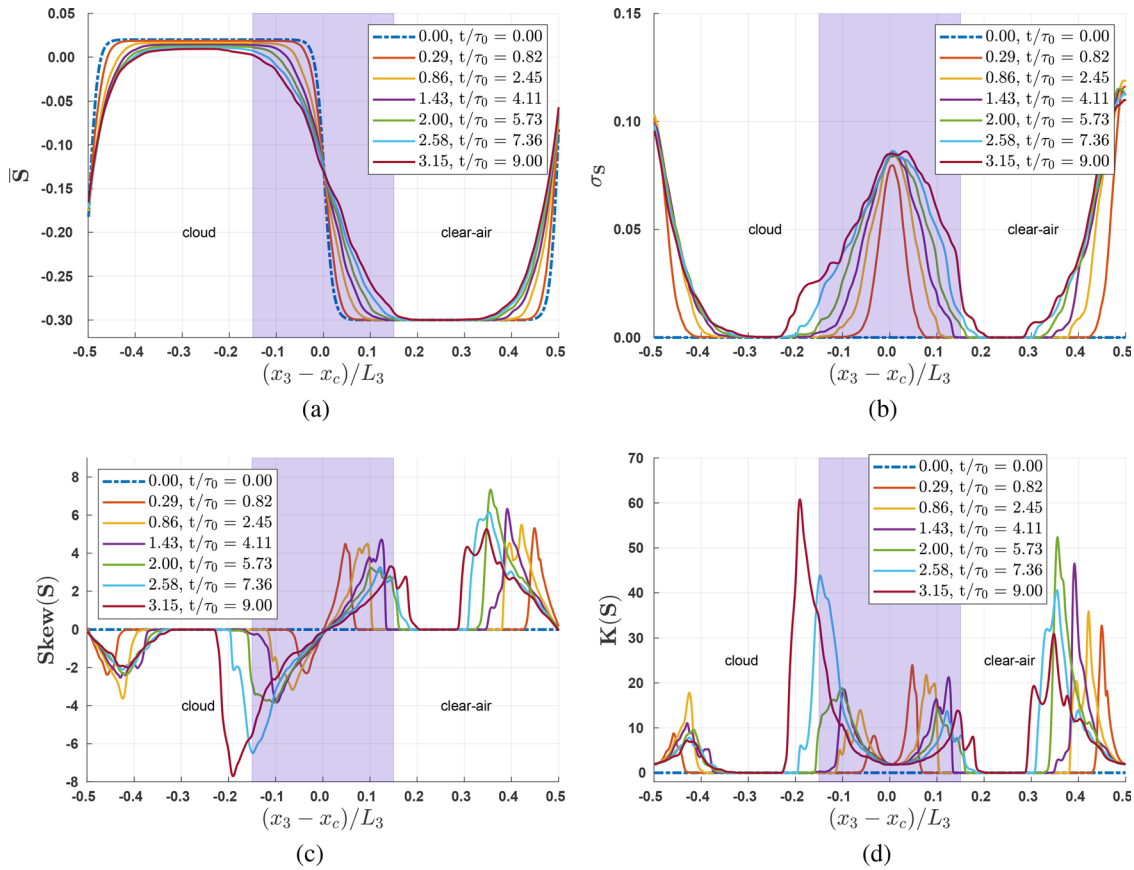


**FIG. 5.** Monodisperse droplet population. Planar averages and statistical moments of supersaturation across the cloudy-under-saturated ambient air interface layer. (a) Supersaturation (or saturation deficit) across the layer. (b) Standard deviation. (c) Skewness. (d) Kurtosis. The initial distributions are plotted with black dash-dotted lines. The approximate extension of the interface mixing layer is indicated as the blue-shaded area between the cloudy and clear air regions.

drops are advected in the upper subsaturated clear-air region. Here, smaller drops will rapidly evaporate and eventually be eliminated by the algorithm. Dissipation rate  $\varepsilon$  decreases during the transient, and heavier droplets are likely to settle, as the small-scale Froude number scales sub-linearly with the dissipation rate  $Fr_\eta \sim \varepsilon^{3/4}$ .<sup>10</sup>

The mean radius plot for the monodisperse case [see Fig. 6(a)] is almost flat in the cloud core region. The extension of this constant-radius plateau becomes more and more reduced as the decaying shearless mixing proceeds. The blue-shaded area represents an approximate extension of the mixing region at the end of the simulated transients. The concentration plots [Fig. 6(b)] display analogous trends. In the polydisperse case, Figs. 6(c) and 6(d), the flat region of nearly constant radii is narrower and presents a peak close to the very top of the mixing layer. This is because collisions are much more frequent in this case. Moreover, given the concomitant presence of very different droplets, the volume ratio between the largest to the smallest droplet is of the order of  $1.25 \times 10^5$ ; thus, the number of collisions is large. Out of a total of  $10^7$  droplets, we in fact observe about  $5 \times 10^4$  collisions over about 8 physical timescales. Information on the collision kernel inside the cloudy and mixing layer regions can be found in Figs. 13 and 14 of Golshan *et al.*<sup>23</sup>

### A. Supersaturation evolution equation and the microphysical timescales

The supersaturation evolution equation has often been used to model a water vapor budget on a developing cloud.<sup>10</sup> This equation is based on a production-condensation model, where the time derivative of supersaturation is determined by balancing a production term,  $\mathcal{P}$ , and a condensation term,  $\mathcal{C}$ .<sup>6,8</sup>

$$\frac{dS}{dt} = \mathcal{P} + \mathcal{C}. \quad (15)$$

The condensation term accounts for the depletion of water vapor and the release of latent heat during condensation at the surface of a spherical droplet, and it is a function of the local level of supersaturation

$$\mathcal{C} = -\frac{S}{\tau_{\text{phase}}} = -4\pi\kappa_v\bar{N}RS. \quad (16)$$

The source term,  $\mathcal{P}$ , has often been modeled as a linear function of the vertical mean velocity of the updraft,<sup>12,15</sup> or identified as the net flux of supersaturated water vapor through the parcel boundaries.<sup>16</sup> In the present analysis, updraft is absent; thus,  $\mathcal{P} = 0$ . Equation (15) does not account for the advection and diffusion of water vapor and



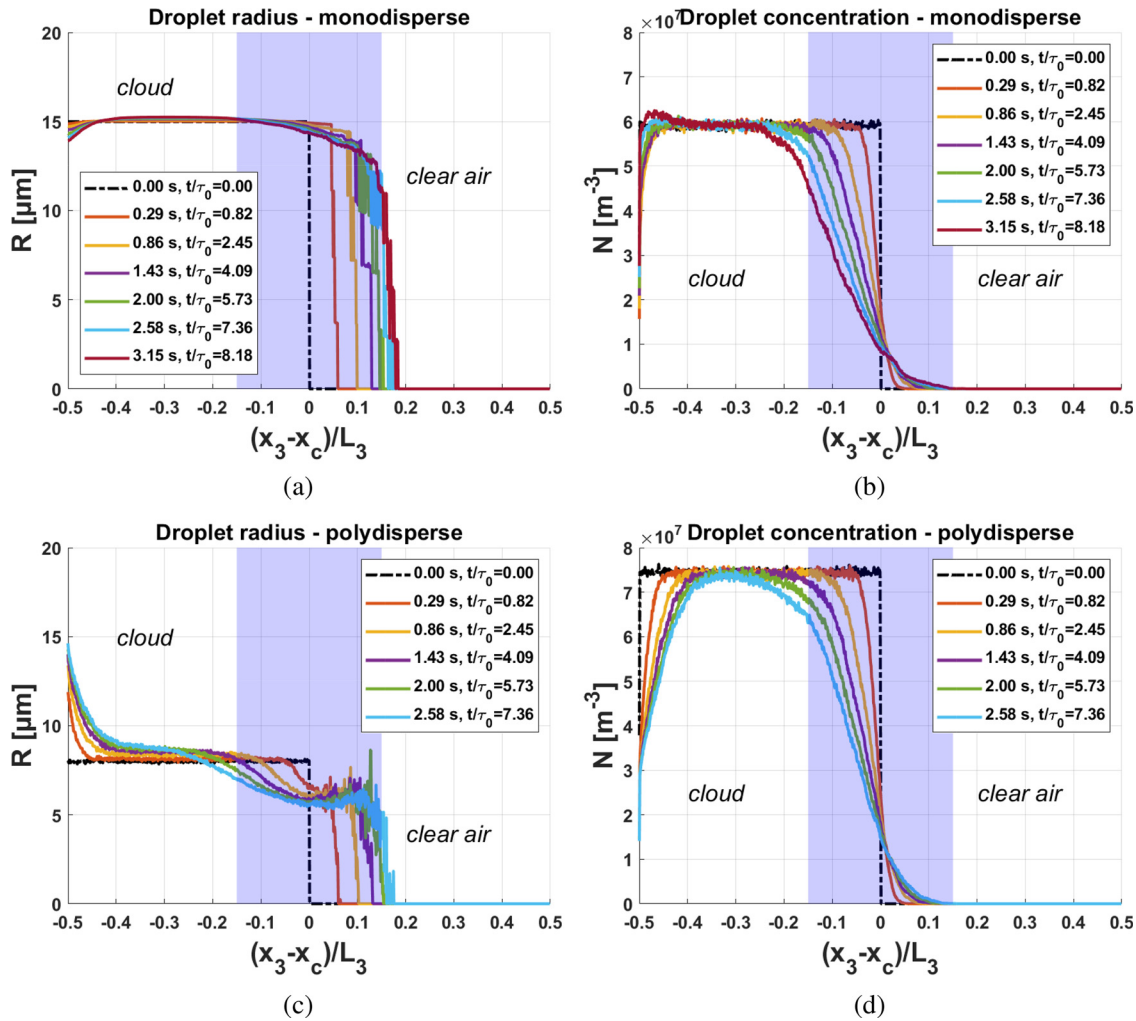


**FIG. 6.** Average mean droplet radius (a) and (c), and concentration (b) and (d). Each value represents the planar average computed for a horizontal plane (see Fig. 1). Shearless mixing takes place in the shaded area. The dash-dotted black line shows the initial conditions.

internal energy in the environment surrounding the droplet ( $Re_{drop} \ll 1$ ) and considers supersaturation  $S$  as a rather global, bulk property of an adiabatic cloud parcel.<sup>7</sup> In their study on cloud cores,<sup>13</sup> generalized the supersaturation evolution equation (15) to a transport model by assuming a linear dependency between the diffusive term of the supersaturation and the Laplacian of the temperature and vapor density fields. They showed that, under steady-state conditions and within the limit of a real-cloud Reynolds' number, the diffusive term of the supersaturation variance becomes negligible.

In a homogeneous, nearly isotropic cloudy layer that is statistically in equilibrium, a zero-mean vertical velocity field would imply a null net vertical transport of cooling vapor parcels. It should be noted that whenever an updraft can be neglected, Eq. (15) can be solved by separating the variables<sup>54</sup>

$$\frac{dS}{dt} \cong -4\pi\kappa_v N \bar{R} S = -\frac{S}{\tau_{phase}}. \quad (17)$$

Therefore, an initially subsaturated (supersaturated), droplet-laden environment experiences an increase (decrease) in the vapor concentration, which results in  $S$  relaxing exponentially to 0. The time constant of this solution is the phase relaxation time

$$\tau_{phase} = (4\pi\kappa_v N \bar{R})^{-1}. \quad (18)$$

The definition of  $\tau_{phase}$  depends on the assumption of the droplet population having a constant integral radius,  $N\bar{R}$ , and it is able to describe the temporal variation of the supersaturation and the liquid water content<sup>5,45</sup> in a homogeneous context. The phase relaxation time was chosen from the microphysical timescales used in several DNS studies that focused on entrainment-mixing processes<sup>4,14,17,19,31</sup> and was used to define the Damköhler number

$$Da = \frac{\tau_{turb}}{\tau_{microphysics}}.$$



Depending on whether the choice of  $\tau_{turb}$  falls into large or small-eddy timescales, a vast range of Damköhler numbers can be defined for the same microphysical timescale in a turbulent flow.<sup>4</sup> Large and small values of  $Da$  are associated with a fast and slow microphysical response of the droplet population to entrainment and turbulent mixing, respectively.<sup>55</sup> Large  $Da$  are also associated with inhomogeneous mixing, whereas small  $Da$  often indicates homogeneous mixing.<sup>2,3</sup>

However, it should be noted that, in a highly anisotropic, inhomogeneous situation, such as inside the mixing layer that separates the cloud from the subsaturated environmental air, the momentum, internal and kinetic energy fluxes, and the water vapor are not zero. The fluxes are positive and rising, forming a peak value that is almost centered in the middle of the layer. Beyond this point, the fluxes decrease and become zero inside the isotropic homogeneous subsaturated ambient air.<sup>26,28,52</sup> In such a situation, a mismatch between the supersaturation time derivative and the condensation term can be expected.

On the other hand, if the focus is on the evolution of the droplet size and the number concentration, the evaporation timescale

offers a good practical description of the process and should be taken as the relevant microphysical timescale,  $\tau_{microphysics}$ . By neglecting the Kelvin and Raoult terms in Eq. (8), and integrating for a constant  $S_0 < 0$ , one can obtain in each computational cell, an estimate of the time required for a single droplet, with an initial radius of  $R_0$ , to evaporate completely in a uniform subsaturated environment

$$\tau_{evap} = -\frac{R_0^2}{2K_s S_0}. \quad (19)$$

Both  $\tau_{phase}$  and  $\tau_{evap}$  rely on the assumption of constant supersaturation and integral radius. However, since both quantities vary concurrently inside a mixing layer, it is better to define a reaction time  $\tau_{react}$ <sup>45</sup> that considers variations of both  $S$  and  $N\bar{R}$ . The reaction time is defined as the shortest time that has elapsed since either the droplet has evaporated completely or the parcel has become saturated, and it is obtained by numerically solving the coupled system of differential equations, that is, Eqs. (8) and (17), for initial non-zero values of positive  $R_0$  and negative  $S_0$ . It should be noted that  $\tau_{evap}$  and  $\tau_{react}$  are only

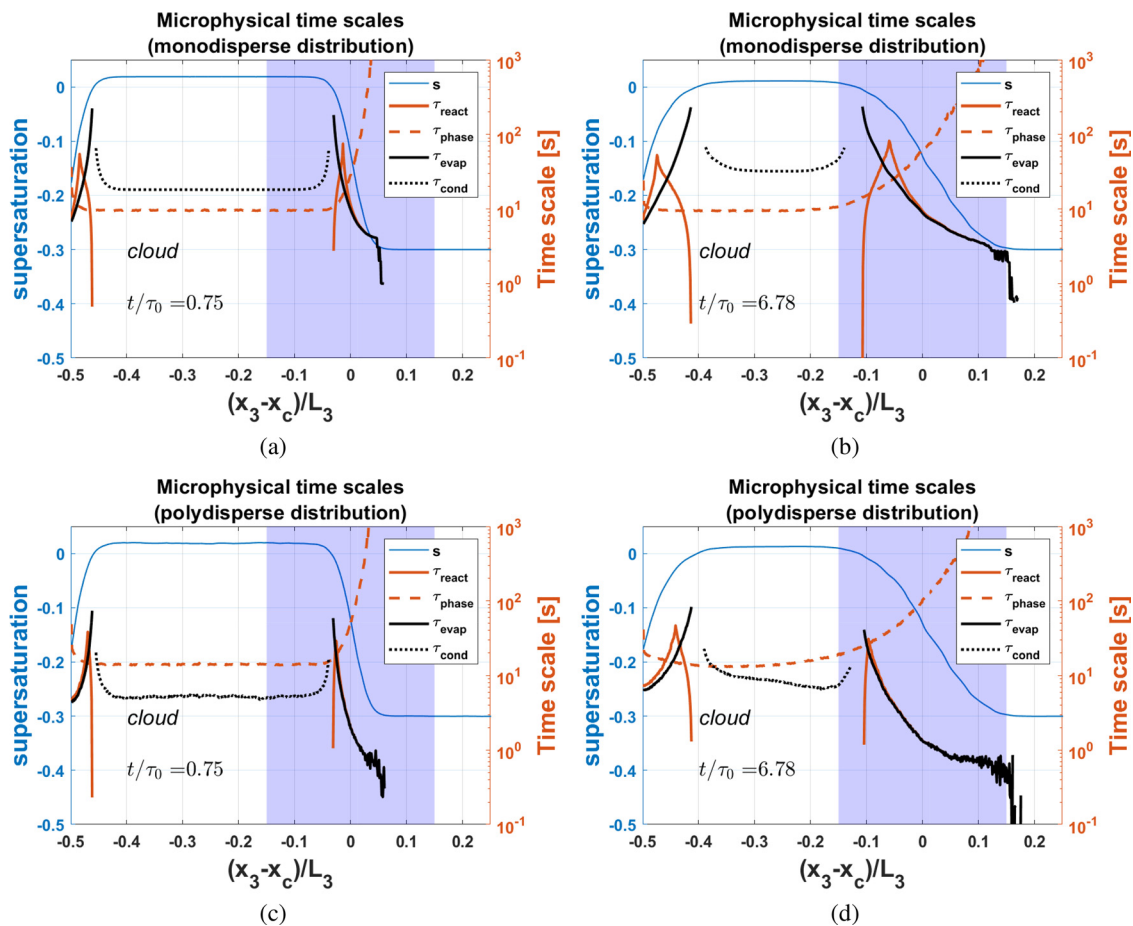


**FIG. 7.** Vertical distribution of the evaporation  $\tau_{evap}$ , phase relaxation  $\tau_{phase}$ , and reaction  $\tau_{react}$  timescales computed inside each grid cell and then averaged on horizontal planes. The data are displayed for the monodisperse (a) and (b), and the polydisperse cases (c) and (d) for two different time steps at the beginning and the end of the transient. The planar average of supersaturation  $S$  [Fig. 5(a)] is also plotted for comparison purposes.

defined for the subsaturated regions, whereas  $\tau_{phase}$  is defined for non-zero values of the integral radius and can also be used in supersaturated regions. In order to describe a characteristic time of the condensation process in supersaturated regions of the domain, we introduce a condensation time  $\tau_{cond}$  which we arbitrarily define as the time it takes a droplet to double its radius for a constant local supersaturation  $S$ ,

$$\tau_{cond} = \frac{3}{2} \frac{R_0^2}{K_s S_0}. \quad (20)$$

The horizontal planar average values of all these microphysical timescales are plotted for two different time instants and the initial droplet size distribution type in the cloud and mixing regions. See Fig. 7, where the computation is performed in each computational grid cell and then averaged over the horizontal planes. For comparison, see also Fig. 8, where the computation is performed by directly using the averaged quantities,  $\bar{R}$  and  $\bar{S}$ . It should be noted that the differently computed quantities are very close, except for the case of the monodisperse population at  $t/\tau = 6.78$ , where the location of the maximum reaction time changes from  $(x_3 - x_c)/L_3 = -0.06$ , Fig. 7, to  $(x_3 - x_c)/L_3 = -0.025$ , Fig. 8.

The condensation and evaporation times diverge toward values of the order of  $10^3$  s at the saturation location,  $S=0$ , where they are not defined, see Fig. 5(a) to observe the displacement in time of the spatial points where  $S=0$ . The phase relaxation time,  $\tau_{phase}$ , elongates across the mixing layer as the mean radius and the droplet concentration (numerical density) decrease. In time, the  $\tau_{phase}$  growth rate smooths out as the layer widens. The fact that  $\tau_{phase}$  grows indefinitely in the diluted interfacial region is not surprising and was also observed during the *in situ* measurements of shallow cumulus clouds by Siebert and Shaw.<sup>15</sup>

It is interesting to observe that, in the monodisperse case, the reaction time is converging to the saturation time (ratio  $\rho_v/\rho_{vs} = 0.995$ ), where the skewness of  $S$  is negative, while it is converging to the evaporation time when  $S$  is positively skewed.

The droplet condensation time is considerably higher everywhere than the phase relaxation time in the monodisperse case and increases in time. The condensation time is instead shorter than the phase relaxation time in the cloudy region in the polydisperse case, but it becomes of the same order as  $\tau_{phase}$  where the mixing process starts. A rise of  $\tau_{cond}$  is observed at the end of the transient in the bottom region of the domain where the sedimentation due to gravity becomes substantial.

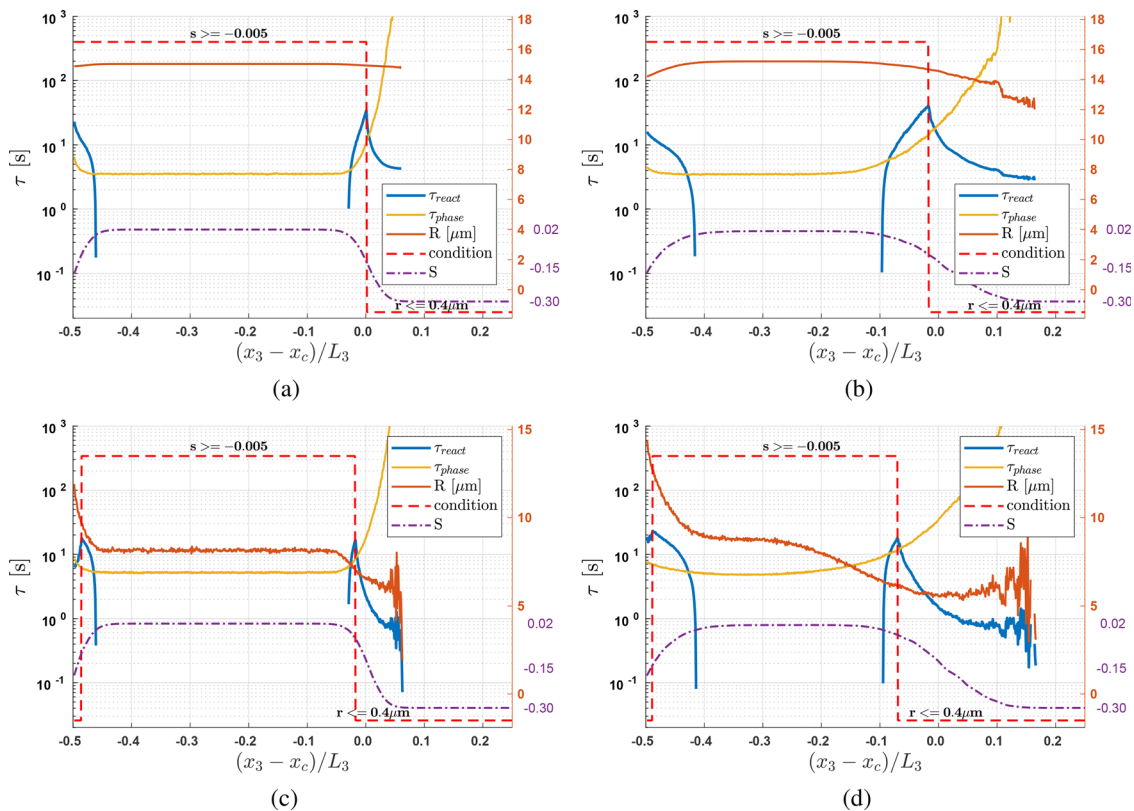


**FIG. 8.** For comparison with Fig. 7, the reaction time and relaxation phase time statistics, computed using planar averaged quantities, are here shown for both polydisperse (c) and (d) and monodisperse (a) and (b) populations and for two different time instants. The red dashed line represents the condition that is first reached at each vertical location when numerically solving the coupled system of Eqs. (8) and (17). Supersaturation  $S$  and the planar averaged  $R$  are included for reading convenience purposes. (a) Monodisperse,  $t/\tau_0 = 0.75$ ; (b) monodisperse,  $t/\tau_0 = 6.61$ ; (c) polydisperse,  $t/\tau_0 = 0.75$ ; and (d) polydisperse,  $t/\tau_0 = 6.61$ .

However, the most interesting observation is that there is a location inside the mixing layer where the phase relaxation, the reaction time, and the evaporation time cluster together. This location precedes the location where the turbulent fluxes maximize. By comparing the distributions in Fig. 7 with the distribution of the turbulent supersaturation flux, see Fig. 9, it is possible to see that the clustering of the microphysical times takes place at almost the same location, where the flux rate is close to a maximum. The microphysical times separate before and after this location. In particular, the reaction time is much shorter than the evaporation and phase relaxation times before this location. The reaction time then collapses to the evaporation time, which is much shorter than the phase relaxation time. In the polydisperse case, the clustering of the microphysical times also includes the condensation time, as expected, since condensation often occurs rapidly in the spectral range of the drops with a small radius for these populations. The evaporation time on the right hand side of the panels in Fig. 7 oscillates to great extent, particularly for the two panels showing the last part of the transient, due to the higher collision rate there. This result should be contrasted with Fig. 2.

### B. Turbulent transport effects on the supersaturation balance

The observed acceleration of the population dynamics in the same cloud–clear air interface region as those studied here, as well as

the rapid differentiation in the size of the droplets, due to the different weights that evaporation, condensation, and collision have in these highly intermittent mixing region,<sup>23</sup> can, at least in part, explain the rapid increase in the size of the droplets that is observed in some cumulus cloud formations, in particular in maritime ones, and which is considered capable of locally inducing rain-fall, Mason and Chien,<sup>56</sup> Li *et al.*<sup>57</sup> These findings have been observed despite the fact that beyond the temporal decay of the turbulence present in the whole system, the interface also hosts the spatial decay of the kinetic energy. It should be considered that the large scales of turbulence vary very little in this flow system, because the computational domain is fixed and because the ratio of the large scales and the ratio of the kinetic energies between the cloudy and ambient air regions vary slowly in time.<sup>24,27</sup> All things considered, these observations lead to the conclusion that the observed accelerated dynamics is associated with the particular small-scale anisotropy and intermittency of the interfacial layer.

In conditions of zero updraft, under almost statistical equilibrium conditions (steady state, homogeneity, and isotropy), the planar averages of the difference between the time derivative of the supersaturation and the condensation terms must be null

$$\overline{dS/dt} - \overline{\mathcal{C}} = \overline{dS/dt} + \overline{S/\tau_p} \cong 0.$$

However, in more general turbulence situations, as in the present system, which is unsteady (a temporal decay follows an initial transient

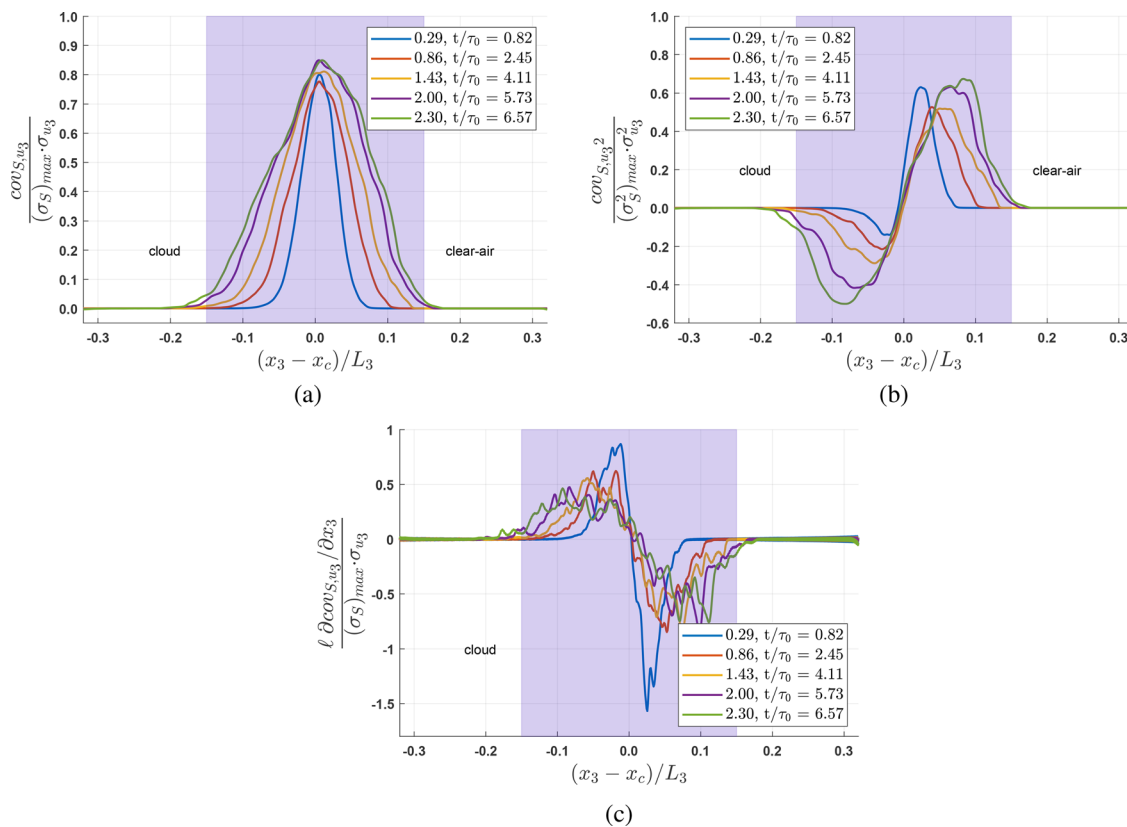


**FIG. 9.** Supersaturation flux statistics for the monodisperse drop population. (a) Normalized covariance (flux) of the supersaturation with vertical velocity component. (b) Normalized covariance of the supersaturation and square of the vertical velocity component. (c) Normalized derivative of the covariance (flux) of the supersaturation with vertical velocity component. The difference of values between the monodisperse and polydisperse population distributions is negligible. The same comparative situation shown in Figs. 5 and 11 holds true.

kinetic energy growth due to an unstable stratification), highly inhomogeneous, and thus anisotropic,  $\overline{dS/dt}$  may not necessarily balance  $\overline{S/\tau_p}$ . This imbalance can be referred to as a turbulence supersaturation fluctuation production,  $\overline{\mathcal{P}_t}$ . As can be seen in Fig. 10,  $\overline{dS/dt} + \overline{S/\tau_p}$  and the covariances between the supersaturation and the longitudinal velocity derivatives along the vertical direction,  $\text{cov}_{S,\partial u_3/\partial x_3}$ , as well as along the horizontal direction  $\text{cov}_{S,\partial u_1/\partial x_1}$ , are plotted across the entire  $(x_3 - x_c)/L_3 \in [-0.5, 0.5]$  domain. All the quantities become larger and almost antisymmetric in the mixing region, and they appear qualitatively skew-symmetric with respect to the central plane  $x_3 \cong x_c$ . It is, thus, evident that, under spatially averaged (planar averages) conditions, the condensation term alone in the supersaturation evolution equation (15) is not able to account for the value of the time derivative of the supersaturation that takes place inside the mixing region.

Provided that the Kolmogorov time,  $\tau_\eta$ , scales with dissipation rate  $\varepsilon$ , the former is found to be much smaller ( $10^{-2}$ – $10^{-1}$  s) than the evaporation and phase relaxation timescales reported in Fig. 7. Large values of  $\tau_{\text{phase}}$  at the interface result in low small-scale Damköhler numbers and should, therefore, enhance turbulent supersaturation fluctuations.<sup>15</sup> It is, therefore, reasonable to assume that supersaturation fluctuations, due to turbulence, are prevalent with respect to those generated by phase transition at the droplet surface. There are two reasons for this hypothesis. First, the statistical moments of the vapor density in an analogous unstable mixing layer with identical initial and boundary conditions and an identical set of control parameters for the carrier flow, but with a subsaturated cloud region where droplets are absent, are close in shape and value to those of mixings that contain droplets coming from a supersaturated cloudy region (see Fig. 8 in Ref. 28).

Second, as can be seen in Figs. 5 and 11, the effects of the supersaturation statistics associated with the different size distributions of

the drop populations are negligible, and the differences are in fact well below 1%. It should be noted that the opposite is not true, that is, that the dynamics of the populations is very sensitive to the shape of the droplet size distribution.

We, therefore, hypothesize that the amplitude of the local supersaturation is modulated by small-scale turbulent fluctuations and that such turbulent fluctuations may contribute to the overall local supersaturation balance. In order to assess this hypothesis, we looked for the proportionality relation between: (i) the difference in the planar averages of the supersaturation time derivative and the condensation term, and (ii) the covariance, Eq. (12), of the supersaturation and the intermittency of the small-scale, as represented by the fluctuations of the longitudinal derivatives of the velocities. In other words, we put

$$\frac{\overline{dS}}{dt} + \frac{\overline{S}}{\tau_{\text{phase}}} = \overline{\mathcal{P}_t} \sim \text{cov}_{S,\partial u_i/\partial x_i}. \quad (21)$$

This is conceptually equivalent to modeling supersaturation production as the product of the supersaturation fluctuations and the characteristic frequency of small-scale turbulent structures,  $\sim \tau_\eta^{-1}$ , where the characteristic frequency of small-scale turbulent motions can be represented by the longitudinal velocity spatial derivatives.

The generation of small-scale anisotropy in turbulent shearless mixing has recently been investigated numerically. Data from direct numerical simulations for Taylor microscale Reynolds numbers between 45 and 150<sup>23–25,28,50</sup> show that there is a significant departure of the longitudinal velocity derivative moments from the values found in homogeneous and isotropic turbulence and that the variation of skewness has the opposite sign for the components across the mixing layer and parallel to it. The anisotropy induced by the presence of a kinetic energy gradient has a very different pattern from the one generated by homogeneous shear. The transversal derivative moments in the mixing are in fact found to be very small, which highlights that smallness of the transversal moments is not a sufficient condition for isotropy. This intermittency is characterized by a large departure of the longitudinal derivative moments (as shown in Fig. 12 together with the supersaturation for two time instances), which are different in direction across and parallel to the layer from the typical values of the isotropic condition, even in such a flow, where there is no energy production (due to the lack of mean flow gradients). The structure of the anisotropy is such that the skewness departure from isotropy reduces the compression on the fluid filaments parallel to the mixing layer and enhances that of the filaments orthogonal to it.

The Pearson correlation coefficient,  $\rho_{\overline{\mathcal{P}_t}, \text{cov}_{S,\partial u_i/\partial x_i}}$ , inside the layer of thickness  $\Delta(t)$ , see Eq. (14), was computed along the transient for  $i = 1, 2, 3$ . The results are shown in Fig. 13, where the data points have been collected for a time increment, that is approximately one half of the initial eddy turnover time.

When the correlation coefficient, that is, the linear correlation between two sets of data, is above 0.7, the correlation is defined as strong. However, we do not expect the numerical simulation to describe the first initial eddy turnover time of the transient accurately. The correlation coefficient decreases slightly along the transient, beyond the first eddy turn over time, as the transient proceeds from values as high as 0.9, when the longitudinal velocity derivative is

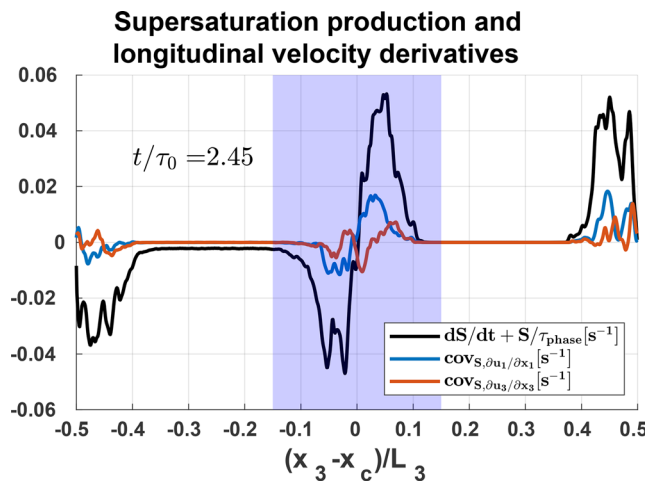


**FIG. 10.** Distribution of the planar horizontal averages along the vertical direction of the difference between the time derivatives of the supersaturation and condensation terms,  $dS/dt - C = dS/dt + S/\tau_p$  and of the covariances  $\text{cov}_{S,\partial u_1/\partial x_1}$ ,  $\text{cov}_{S,\partial u_3/\partial x_3}$ , see Eq. (12). These quantities vary considerably inside the mixing layer, and the two kinds of curves are both almost antisymmetric with respect to the center of mixing layer  $x_c$ . The data were retrieved from a monodisperse simulation at  $t/\tau_0 = 2.45$ .



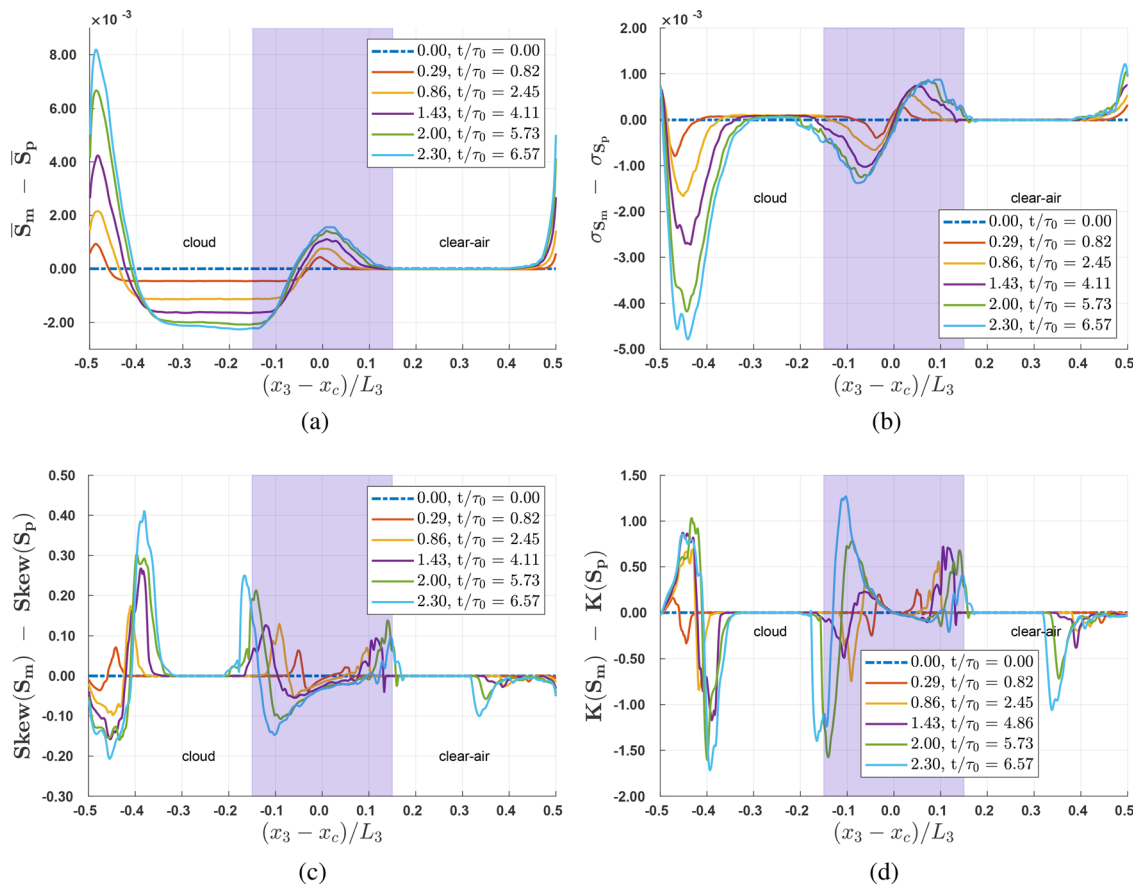


**FIG. 11.** Difference in the supersaturation statistics between monodisperse ( $S_m$ ) and polydisperse ( $S_p$ ) droplet populations across the cloudy–under-saturated ambient air interface layer. (a) Difference in the mean supersaturation (or saturation deficit) across the layer. (b) Difference in the standard deviation. (c) Difference in the skewness. (d) Difference in the kurtosis. The approximate extension of the interface mixing layer is indicated as the blue shaded area between the cloudy and clear air regions.

horizontal, and as high as 0.8, when the longitudinal velocity derivative is vertical, to values close to 0.7. This is true for both monodisperse and polydisperse drop populations.

The relatively large absolute values of the correlation coefficients confirm that a quasi-linear relation should hold between the source term  $\overline{\mathcal{P}_t}$  and  $\text{cov}_{S\partial u_i/\partial x_i}$ . An alternative way of estimating the proportionality constant,  $C$ , relevant to the dimensional quantities, along the transient is to integrate across the mixing layer of  $\overline{\mathcal{P}_t}$  and  $\text{cov}_{S\partial u_i/\partial x_i}$ ,  $i = 1, 2$ :

$$\int_{\Delta} \left| \frac{d\bar{S}}{dt} + \frac{\bar{S}}{\tau_{\text{phase}}} \right| dx_3 \cong C \int_{\Delta} |\text{cov}_{S\partial u_i/\partial x_i}| dx_3.$$

The estimated values of the non-dimensional constant  $C$  are reported in Fig. 13 (orange curve). Once again, the shape of the initial droplet size distribution does not seem to affect either the evolution of the correlation coefficient or the non-dimensional constant  $C$  during the transient. In all these cases, the estimated value is 5, an asymptotic value, that is rapidly reached after the first initial eddy turnover. We can observe a different pre-asymptotic trend for the horizontal and

vertical longitudinal derivative correlation coefficients, which is due to the intrinsic small-scale anisotropy of the mixing layer between the cloudy region and the clear-air, see the discussion above.

#### IV. CONCLUSIONS

We have considered the relationship between supersaturation fluctuations and turbulent small-scale dynamics in the context of an inhomogeneous, anisotropic, shearless, turbulent air mixing layer, which is often used to model the carrier flow at the interface between warm clouds and unsaturated environmental air. Two initial droplet population types, that is, a  $15\text{ }\mu\text{m}$ -monodisperse one and constant-mass-per-volume-class polydisperse one, were tested.

The various timescales pertaining to the microphysics of a droplet population were compared inside the top of the cloudy region, the layer where the turbulent transport process toward the environmental subsaturated air takes place. The evaporation, reaction, and phase relaxation timescales match for a value close to 20–30 s inside the layer just before the location where the supersaturation flux reaches its maximum rate of variation. In the case of a polydisperse population, this



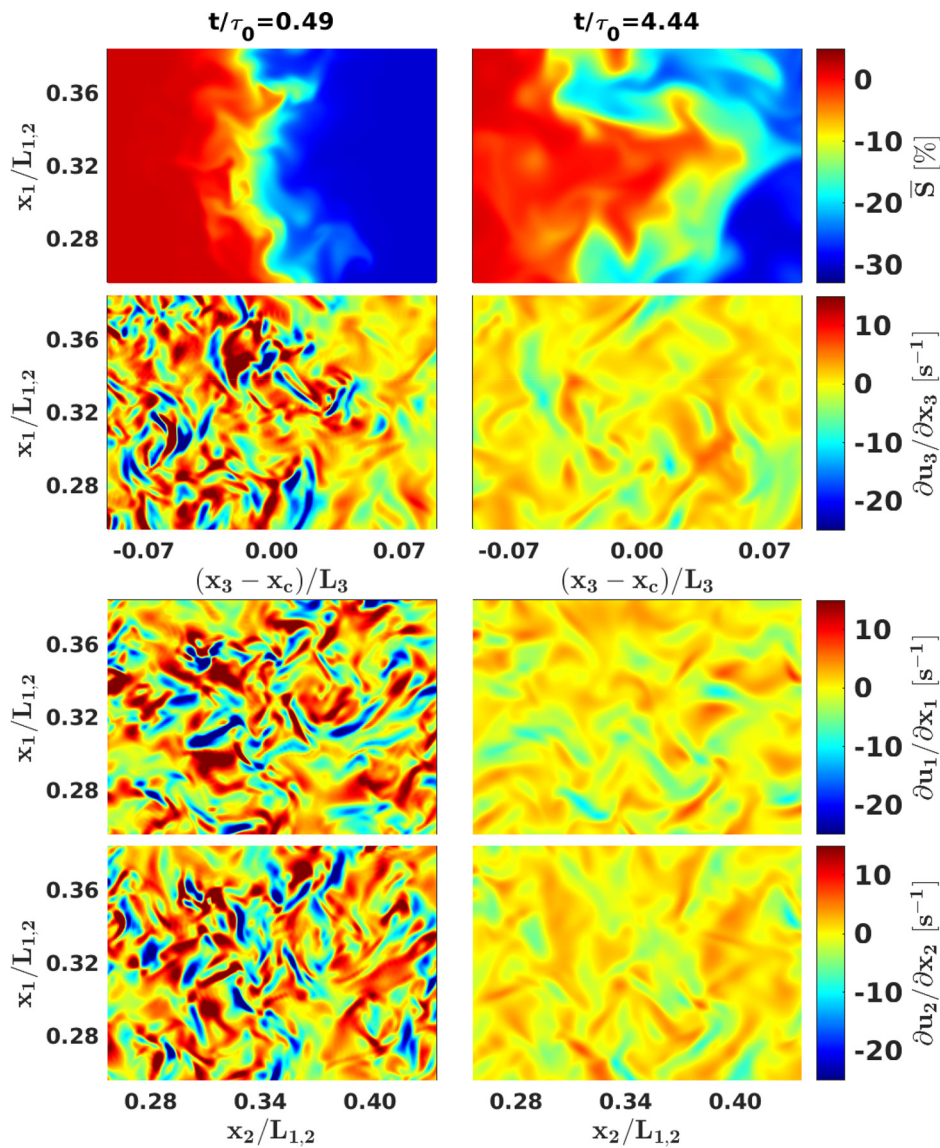


**FIG. 12.** Visualizations of the supersaturation (top row) and longitudinal velocity derivatives in the mixing region (second, third, and fourth rows). The plots display only a portion of the domain, as shown by the normalized coordinates at two time instances  $t/\tau_0 = 0.49$  and  $t/\tau_0 = 4.44$ .  $x_c$  denotes the initial position of the mixing layer. The variance of the longitudinal velocity derivatives is of the order of  $10 \text{ s}^{-1}$  at the beginning of the transient, but rapidly decreases. The values of the inverse Kolmogorov times in the mixing region are plotted in Fig. 4(c) (indigo dash-dotted line) and are of the same order of magnitude as the derivatives shown in this figure.

match includes the condensation time. The timescales before this spatial location are different, with differences of the order of one minute. Beyond this location, the evaporation and reaction times overlap, while the relaxation phase and condensation timescales asymptotically diverge, since the environment becomes more and more undersaturated.

Under the hypothesis of the supersaturation fluctuation depending on a great extent on the small-scale intermittency of the carrier flow that hosts the vapor and liquid water phases, we have analyzed the supersaturation balance equation with the aim of evincing their reciprocal correlation. In order to assess this hypothesis, we compared the estimated planar averages of the time derivative of the supersaturation and the condensation terms with the planar covariance of the supersaturation and the longitudinal

velocity derivatives. The statistics of the velocity derivatives are in fact particularly relevant for small-scale dynamics. For the specific shearless turbulent structure considered here, the longitudinal velocity derivatives are more significant for small-scale intermittency than the transversal ones, which are null. Moreover, the longitudinal velocity derivative can be considered as a characteristic measure of the small-scale frequency,  $\tau_\eta^{-1}$ . We have found a high value of the Pearson correlation coefficient,  $\rho_{\overline{\mathcal{P}_1}, \text{cov} S \partial u_1 / \partial x_1} \sim 0.7$  for the droplet populations, both inside the interfacial layer and along the entire simulation transient, which leads to the conclusion that, in the absence of an updraft, the mismatch of the time derivative of the supersaturation and the condensation terms is linearly related to the covariance of the supersaturation and the longitudinal velocity derivatives of the carrier flow.

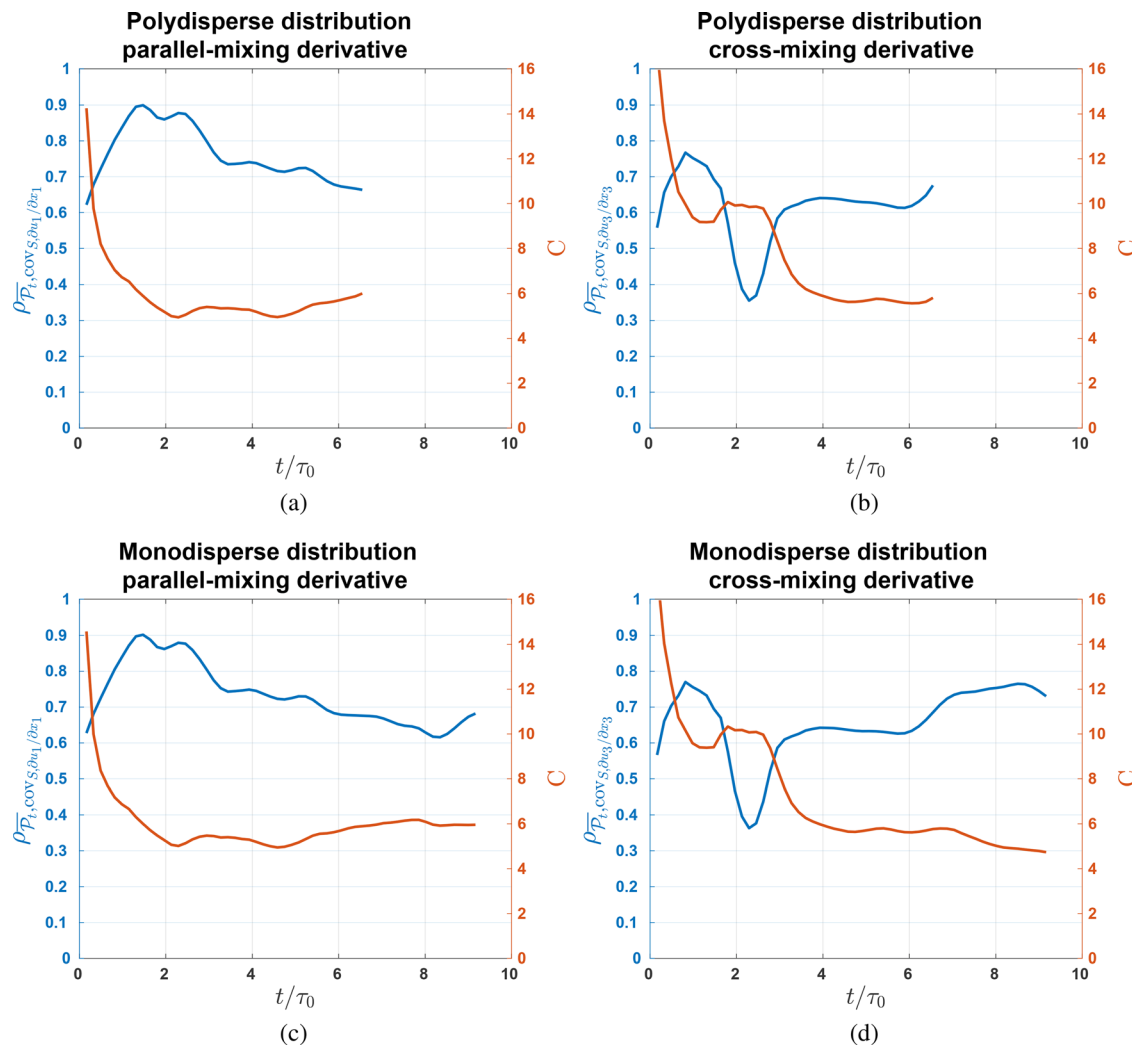


**FIG. 13.** Time evolution of the estimated production-planar covariance correlation coefficient and the proportionality constant. The Pearson correlation coefficient between the turbulence production term  $\mathcal{P}_t$ , see Eq. (21), and the supersaturation-velocity longitudinal derivative covariance (blue curves) plotted for the horizontal [left, (a) and (c)] and vertical [right, (b) and (d)] longitudinal derivatives during the transient. The correlation coefficient peaks around the first initial eddy turnover time and slowly decreases in magnitude to an asymptote  $\sim 0.7$  as the transient progresses.

## ACKNOWLEDGMENTS

This project has received funding from the Marie-Sklodowska Curie Actions (MSCA ITN ETN COMPLETE) under the European Union's Horizon 2020 research and innovation program. Grant Agreement No. 675675, <http://www.complete-h2020network.eu>. We acknowledge Cineca-Supercomputer Applications and Innovations (SCAI) for providing the computational resources and technical support on Marconi Tier-0 system under ISCRA project No. HP10CA2ZRB. The post-processing activity was in part conducted on the HACTAR cluster, and the computational resources were provided by HPC@POLITO, a project of Academic Computing within the Department of Control and Computer Engineering at the Politecnico di Torino (<http://www.hpc.polito.it>). We also thank J. Schumacher (Imlneau University of Technology) for useful discussions.

## AUTHOR DECLARATIONS

### Conflict of Interest

The authors have no conflicts to disclose.

## DATA AVAILABILITY

The data that support the findings of this study are available from the corresponding author upon reasonable request.

## REFERENCES

1. J. Warner, "The microstructure of cumulus cloud. Part I. General features of the droplet spectrum," *J. Atmos. Sci.* **26**, 1049–1059 (1969).
2. J. Latham and R. L. Reed, "Laboratory studies of the effects of mixing on the evolution of cloud droplet spectra," *Q. J. R. Meteorol. Soc.* **103**, 297–306 (1977).

- <sup>3</sup>M. B. Baker, R. G. Corbin, and J. Latham, "The influence of entrainment on the evolution of cloud droplet spectra: I. A model of inhomogeneous mixing," *Q. J. R. Meteorol. Soc.* **106**, 581–598 (1980).
- <sup>4</sup>B. Kumar, J. Schumacher, and R. A. Shaw, "Cloud microphysical effects of turbulent mixing and entrainment," *Theor. Comput. Fluid Dyn.* **27**, 361–376 (2013).
- <sup>5</sup>C. Lu, Y. Liu, B. Zhu, S. S. Yum, S. K. Krueger, Y. Qiu, S. Niu, and S. Luo, "On which microphysical time scales to use in studies of entrainment-mixing mechanisms in clouds," *J. Geophys. Res.: Atmos.* **123**, 3740–3756, <https://doi.org/10.1002/2017JD027985> (2018).
- <sup>6</sup>P. Squires, "The growth of cloud drops by condensation. I. General characteristics," *Aust. J. Chem.* **5**, 59–86 (1952).
- <sup>7</sup>R. Rogers and M. Yau, *A Short Course in Cloud Physics* (Elsevier Science, 1996).
- <sup>8</sup>S. Twomey, "The nuclei of natural cloud formation part II: The supersaturation in natural clouds and the variation of cloud droplet concentration," *Geofis. Pura Appl.* **43**, 243–249 (1959).
- <sup>9</sup>M. K. Politovich and W. A. Cooper, "Variability of the supersaturation in cumulus clouds," *J. Atmos. Sci.* **45**, 1651–1664 (1988).
- <sup>10</sup>B. J. Devenish, P. Bartello, J.-L. Brenguier, L. R. Collins, W. W. Grabowski, R. H. A. IJzermans, S. P. Malinowski, M. W. Reeks, J. C. Vassilicos, L.-P. Wang, and Z. Warhaft, "Droplet growth in warm turbulent clouds," *Q. J. R. Meteorol. Soc.* **138**, 1401–1429 (2012).
- <sup>11</sup>W. W. Grabowski and L.-P. Wang, "Growth of cloud droplets in a turbulent environment," *Annu. Rev. Fluid Mech.* **45**, 293–324 (2013).
- <sup>12</sup>W. A. Cooper, "Effects of variable droplet growth histories on droplet size distributions. Part I: Theory," *J. Atmos. Sci.* **46**, 1301–1311 (1989).
- <sup>13</sup>G. Sardina, F. Picano, L. Brandt, and R. Caballero, "Continuous growth of droplet size variance due to condensation in turbulent clouds," *Phys. Rev. Lett.* **115**, 184501 (2015).
- <sup>14</sup>K. K. Chandrakar, W. Cantrell, K. Chang, D. Ciochetto, D. Niedermeier, M. Ovchinnikov, R. A. Shaw, and F. Yang, "Aerosol indirect effect from turbulence-induced broadening of cloud-droplet size distributions," *Proc. Natl. Acad. Sci.* **113**, 14243–14248 (2016).
- <sup>15</sup>H. Siebert and R. A. Shaw, "Supersaturation fluctuations during the early stage of cumulus formation," *J. Atmos. Sci.* **74**, 975–988 (2017).
- <sup>16</sup>P. Prabhakaran, A. S. M. Shawon, G. Kinney, S. Thomas, W. Cantrell, and R. A. Shaw, "The role of turbulent fluctuations in aerosol activation and cloud formation," *Proc. Natl. Acad. Sci.* **117**, 16831–16838 (2020).
- <sup>17</sup>B. Kumar, J. Schumacher, and R. A. Shaw, "Lagrangian mixing dynamics at the cloudy-clear air interface," *J. Atmos. Sci.* **71**, 2564–2580 (2014).
- <sup>18</sup>Z. Gao, Y. Liu, X. Li, and C. Lu, "Investigation of turbulent entrainment-mixing processes with a new particle-resolved direct numerical simulation model," *J. Geophys. Res.: Atmos.* **123**, 2194–2214, <https://doi.org/10.1002/2017JD027507> (2018).
- <sup>19</sup>B. Kumar, P. Götzfried, N. Suresh, J. Schumacher, and R. A. Shaw, "Scale dependence of cloud microphysical response to turbulent entrainment and mixing," *J. Adv. Model. Earth Syst.* **10**, 2777–2785 (2018).
- <sup>20</sup>R. S. Miller and J. Bellan, "Direct numerical simulation and subgrid analysis of a transitional droplet laden mixing layer," *Phys. Fluids* **12**, 650–671 (2000).
- <sup>21</sup>R. Onishi, K. Takahashi, and S. Komori, "Influence of gravity on collisions of monodispersed droplets in homogeneous isotropic turbulence," *Phys. Fluids* **21**, 125108 (2009).
- <sup>22</sup>R. S. Sidin, R. H. A. IJzermans, and M. W. Reeks, "A lagrangian approach to droplet condensation in atmospheric clouds," *Phys. Fluids* **21**, 106603 (2009).
- <sup>23</sup>M. Golshan, S. Abdunabiev, M. Tomatis, F. Fraternali, M. Vanni, and D. Tordella, "Intermittency acceleration of water droplet population dynamics inside the interfacial layer between cloudy and clear air environments," *Int. J. Multiphase Flow* **140**, 103669 (2021).
- <sup>24</sup>D. Tordella and M. Iovieno, "Small-scale anisotropy in turbulent shearless mixing," *Phys. Rev. Lett.* **107**, 194501 (2011).
- <sup>25</sup>D. Tordella and M. Iovieno, "Decaying turbulence: What happens when the correlation length varies spatially in two adjacent zones," *Physica D* **241**, 178–185 (2012).
- <sup>26</sup>D. Tordella, M. Iovieno, and P. R. Bailey, "Sufficient condition for Gaussian departure in turbulence," *Phys. Rev. E* **77**, 016309 (2008).
- <sup>27</sup>D. Tordella and M. Iovieno, "Numerical experiments on the intermediate asymptotics of shear-free turbulent transport and diffusion," *J. Fluid Mech.* **549**, 429–441 (2006).
- <sup>28</sup>L. Gallana, S. Abdunabiev, M. Golshan, and D. Tordella, "Diffusion of turbulence following both stable and unstable step stratification perturbations," *arXiv:2201.06920* (2022).
- <sup>29</sup>P. A. Vaillancourt, M. K. Yau, and W. W. Grabowski, "Microscopic approach to cloud droplet growth by condensation. Part I: Model description and results without turbulence," *J. Atmos. Sci.* **58**, 1945–1964 (2001).
- <sup>30</sup>M. Andrejczuk, W. W. Olshanrabowski, S. P. Malinowski, and P. K. Smolarkiewicz, "Numerical simulation of cloud-clear air interfacial mixing," *J. Atmos. Sci.* **61**, 1726–1739 (2004).
- <sup>31</sup>P. Götzfried, B. Kumar, R. A. Shaw, and J. Schumacher, "Droplet dynamics and fine-scale structure in a shearless turbulent mixing layer with phase changes," *J. Fluid Mech.* **814**, 452–483 (2017).
- <sup>32</sup>D. Tritton, *Physical Fluid Dynamics* (Oxford Science Publications, Clarendon Press, 1988).
- <sup>33</sup>P. J. Ireland and L. R. Collins, "Direct numerical simulation of inertial particle entrainment in a shearless mixing layer," *J. Fluid Mech.* **704**, 301–332 (2012).
- <sup>34</sup>R. A. Shaw, "Particle-turbulence interactions in atmospheric clouds," *Annu. Rev. Fluid Mech.* **35**, 183–227 (2003).
- <sup>35</sup>P. G. Saffman and J. S. Turner, "On the collision of drops in turbulent clouds," *J. Fluid Mech.* **1**, 16–30 (1956).
- <sup>36</sup>L. P. Wang, A. S. Wexler, and Y. Zhou, "Statistical mechanical description and modelling of turbulent collision of inertial particles," *J. Fluid Mech.* **415**, 117–153 (2000).
- <sup>37</sup>K. K. Chandrakar, I. Saito, F. Yang, W. Cantrell, T. Gotoh, and R. A. Shaw, "Droplet size distributions in turbulent clouds: Experimental evaluation of theoretical distributions," *Q. J. R. Meteorol. Soc.* **146**, 483–504 (2020).
- <sup>38</sup>S. J. Ghan, H. Abdul-Razzak, A. Nenes, Y. Ming, X. Liu, M. Ovchinnikov, B. Shipway, N. Meskhidze, J. Xu, and X. Shi, "Droplet nucleation: Physically-based parameterizations and comparative evaluation," *J. Adv. Model. Earth Syst.* **3**, M10001 (2011).
- <sup>39</sup>H. Pruppacher and J. Klett, *Microphysics of Clouds and Precipitation*, Atmospheric and Oceanographic Sciences Library (Springer, Netherlands, 2010).
- <sup>40</sup>R. Rogers, "Raindrop collision rate," *J. Atmos. Sci.* **46**, 2469–2472 (1989).
- <sup>41</sup>S. Balachandar and J. K. Eaton, "Turbulent dispersed multiphase flow," *Annu. Rev. Fluid Mech.* **42**, 111–133 (2010).
- <sup>42</sup>J. I. MacPherson and G. A. Isaac, "Turbulent characteristics of some Canadian cumulus clouds," *J. Appl. Meteorol.* **16**, 81–90 (1977).
- <sup>43</sup>H. Siebert, K. Lehmann, and M. Wendisch, "Observations of small-scale turbulence and energy dissipation rates in the cloudy boundary layer," *J. Atmos. Sci.* **63**, 1451–1466 (2006).
- <sup>44</sup>H. Siebert, R. A. Shaw, and Z. Warhaft, "Statistics of small-scale velocity fluctuations and internal intermittency in marine stratocumulus clouds," *J. Atmos. Sci.* **67**, 262–273 (2010).
- <sup>45</sup>K. Lehmann, H. Siebert, and R. A. Shaw, "Homogeneous and inhomogeneous mixing in cumulus clouds: Dependence on local turbulence structure," *J. Atmos. Sci.* **66**, 3641–3659 (2009).
- <sup>46</sup>H. Siebert, S. Gershchenko, A. Gylfason, K. Lehmann, L. Collins, R. Shaw, and Z. Warhaft, "Towards understanding the role of turbulence on droplets in clouds: In situ and laboratory measurements," *Atmos. Res.* **97**, 426–437 (2010).
- <sup>47</sup>S. B. Pope, *Turbulent Flows* (Cambridge University Press, 2000).
- <sup>48</sup>T. Ishihara, T. Gotoh, and Y. Kaneda, "Study of high-Reynolds number isotropic turbulence by direct numerical simulation," *Annu. Rev. Fluid Mech.* **41**, 165–180 (2009).
- <sup>49</sup>M. Iovieno, C. Cavazzoni, and D. Tordella, "A new technique for a parallel dealiased pseudospectral Navier-Stokes code," *Comput. Phys. Commun.* **141**, 365–374 (2001).
- <sup>50</sup>M. Iovieno, S. D. Savino, L. Gallana, and D. Tordella, "Mixing of a passive scalar across a thin shearless layer: Concentration of intermittency on the sides of the turbulent interface," *J. Turbul.* **15**, 311–334 (2014).

- <sup>51</sup>K. A. Brucker, J. C. Isaza, T. Vaithianathan, and L. R. Collins, “Efficient algorithm for simulating homogeneous turbulent shear flow without remeshing,” *J. Comput. Phys.* **225**, 20–32 (2007).
- <sup>52</sup>S. Veeravalli and Z. Warhaft, “The shearless turbulence mixing layer,” *J. Fluid Mech.* **207**, 191–229 (1989).
- <sup>53</sup>L. Djenidi, M. Kamruzzaman, and R. Antonia, “Power-law exponent in the transition period of decay in grid turbulence,” *J. Fluid Mech.* **779**, 544–555 (2015).
- <sup>54</sup>V. Khvorostyanov and J. Curry, *Thermodynamics, Kinetics, and Microphysics of Clouds* (Cambridge University Press, 2014).
- <sup>55</sup>M. Andrejczuk, W. W. Grabowski, S. P. Malinowski, and P. K. Smolarkiewicz, “Numerical simulation of cloud–clear air interfacial mixing: Homogeneous versus inhomogeneous mixing,” *J. Atmos. Sci.* **66**, 2493–2500 (2009).
- <sup>56</sup>B. Mason and C. Chien, “Cloud-droplet growth by condensation in cumulus,” *Q. J. R. Meteorol. Soc.* **88**, 136–142 (1962).
- <sup>57</sup>X.-Y. Li, A. Brandenburg, G. Svensson, N. E. L. Haugen, B. Mehlig, and I. Rogachevskii, “Condensational and collisional growth of cloud droplets in a turbulent environment,” *J. Atmos. Sci.* **77**, 337–353 (2020).